Atmospheric dynamics II

Planetary-scale atmospheric circulation

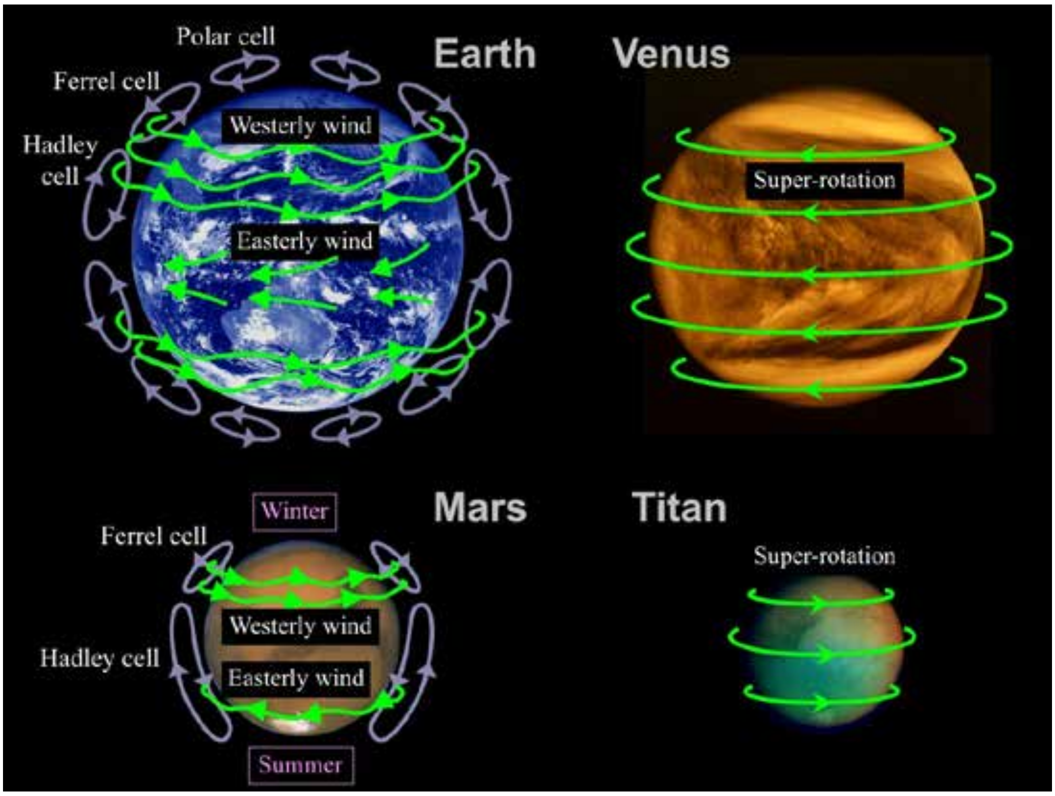

Baroclinic wave disturbances

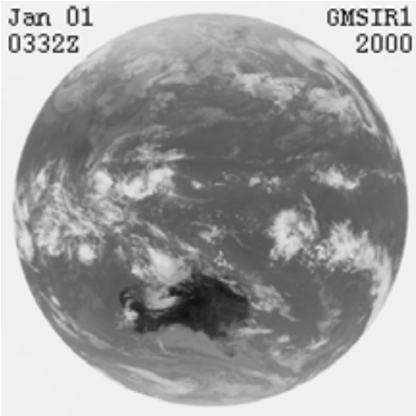

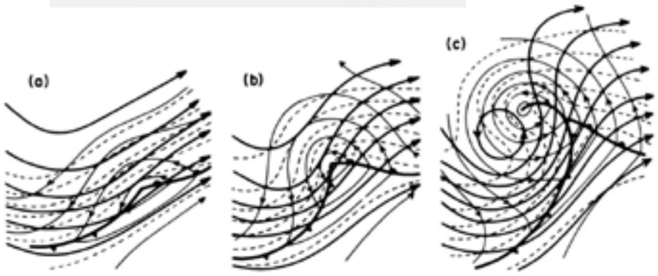

Fig. 6.5 Schematic 500-hPa contours (heavy solid lines), 1000-hPa contours (thin lines), and 1000–500 hPa thickness (dashed) for a developing baroclinic wave at three stages of development. (After Palmén and Newton, 1969.)

Holton 2012

Frontal dust storms on Mars
(Wang et al. 2005)

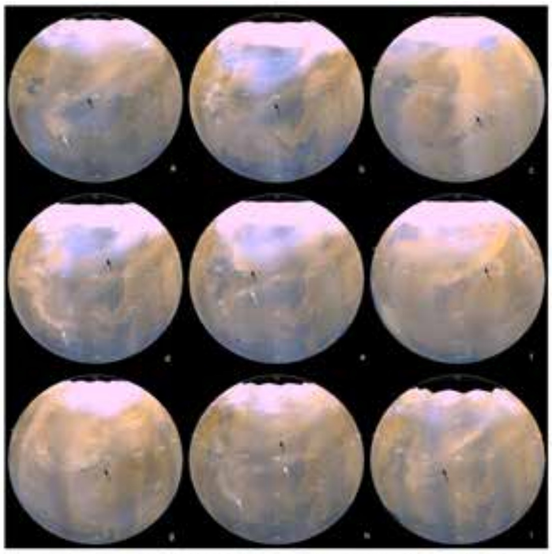

Figure 5. Examples of flushing dust storms in different channels, seasons, and years. Each panel is a Mars daily global map projected onto a sphere with black arrows pointing to the main frontal features. The three rows from the top to the bottom are for MGS mapping Years 1 (1999–2001), 2 (2001–2003), and 3 (2003–2005), respectively. Figures 5a, 5b, 5d, 5e, 5h, and 5i are for the Acidalia channel. Figure 5c is for the Arcadia channel. Figures 5f and 5g are for the Utopia channel. The *Ls* values are (a) 210°, (b) 314°, (c) 336°, (d) 316°, (e) 324°, (f) 324°, (g) 207°, (h) 214°, and (i) 230°.

Eady stability problem for baroclinic disturbances

The structures of unstable modes in a simplified atmosphere with a north-south temperature gradient

- f -plane (β = 0).
- ∂U/∂z = constant.
- Rigid lids at z = 0 and H

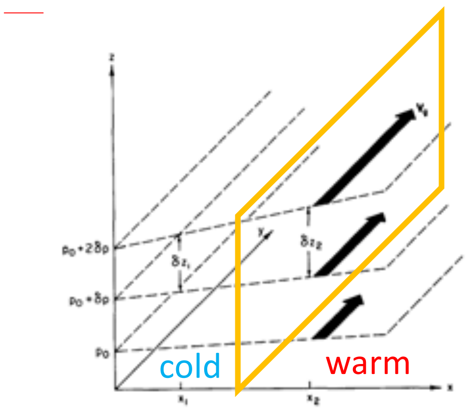

Fig. 3.8 Relationship between vertical shear of the geostrophic wind and horizontal temperature gradients. (Note: $\delta p < 0$.)

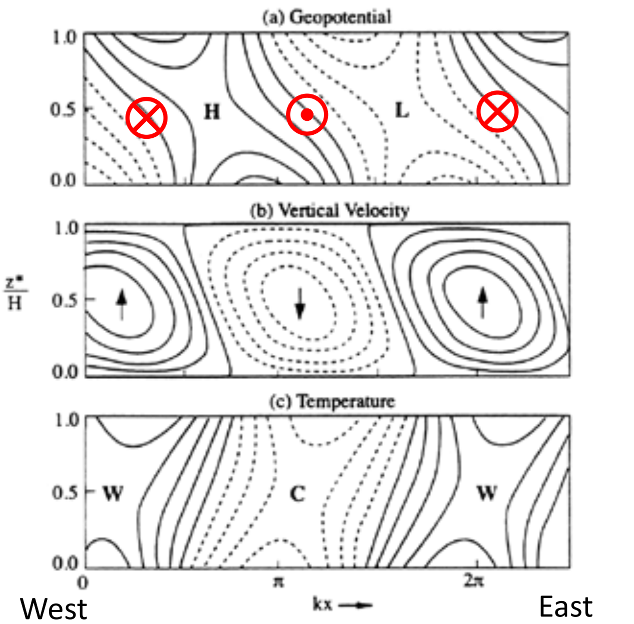

Fig. 8.10 Properties of the most unstable Eady wave. (a) Contours of perturbation geopotential height; *H* and *L* designate ridge and trough axes, respectively. (b) Contours of vertical velocity; up and down arrows designate axes of maximum upward and downward motion, respectively. (c) Contours of perturbation temperature; W and C designate axes of warmest and coldest temperatures, respectively. In all panels 1 and 1/4 wavelengths are shown for clarity.

Holton (2004)

3D structure of baroclinic wave disturbance (→ Ferrel cell)

（伊藤 1976）

rising warm air to the east of trough & subsidence of cold air to the west of trough
→ conversion from eddy potential energy to eddy kinetic energy

cold advection below trough → development of trough
warm advection below ridge → development of ridge

Meridional heat transport

$\overline{v'T'}$

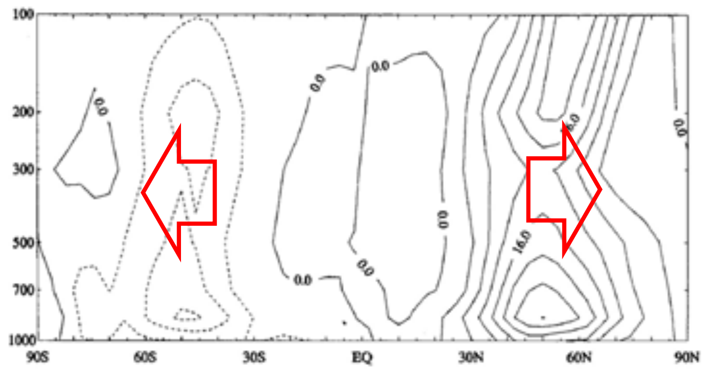

Fig. 10.3 Observed northward eddy heat flux distribution (°C m s^{-1}) for Northern Hemisphere winter. (Adapted from Schubert et al., 1990.)

stream function

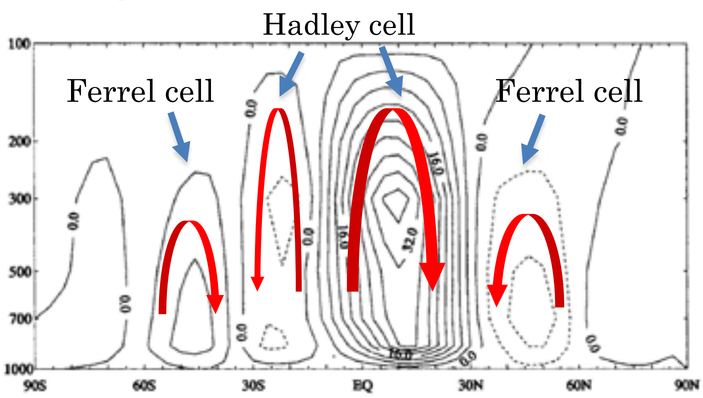

Holton 2004

Fig. 10.7 Streamfunction (units: 10^2 kg m^{-1}s^{-1}) for the observed Eulerian mean meridional circulation for Northern Hemisphere winter, based on the data of Schubert et al. (1990).

Surface meteorological measurements on Mars by Viking-2

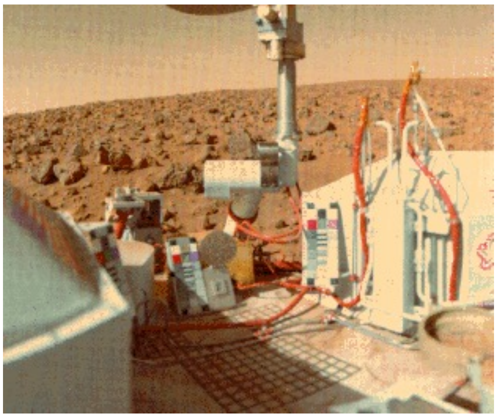

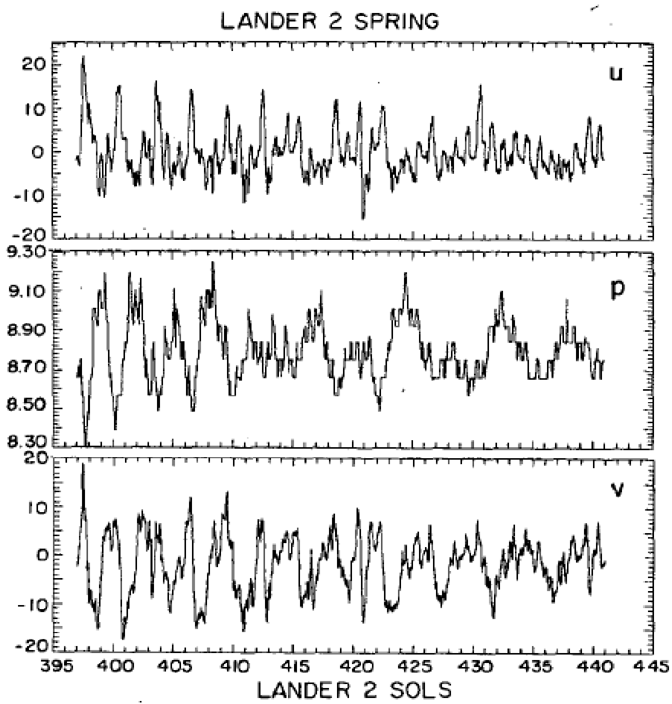

(Barnes, 1980)

FIG. 2. The unfiltered pressure and zonal (u) and meridional (v) wind data for a 44-sol portion of the spring period at Lander 2. The pressure is in mb, with the wind speeds in m s^{-1}.

Meridional circulation in a Martian GCM (general circulation model)

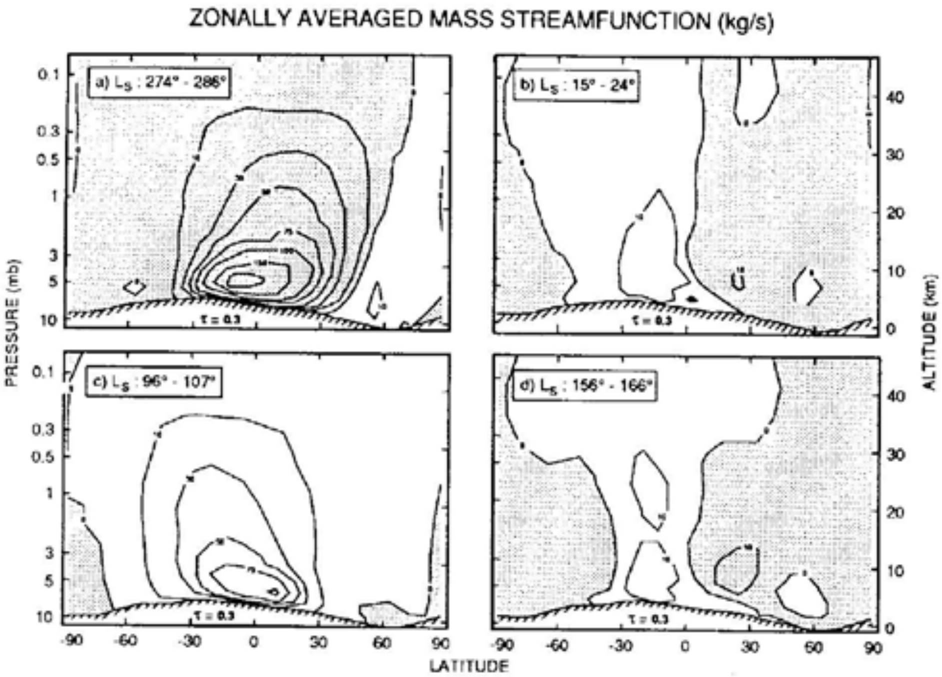

Fig. 19. Mass-weighted stream functions computed by the Mars-GCM (Pollack et al. 1990a) for early northern winter (a: $L_s \approx 280°$), early northern spring (b: $L_s \approx 20°$), early northern summer (c: $L_s \approx 103°$) and late northern summer (d: $L_s \approx 161°$). A background dust opacity of τ = 0.3 was assumed. Flow in the meridional plane is clockwise around minima (negative values are shaded) and anti-clockwise around maxima; winds are strongest where contours are closest.

(Pollack et al 1990)

Baroclinic instability in Venusian atmosphere?

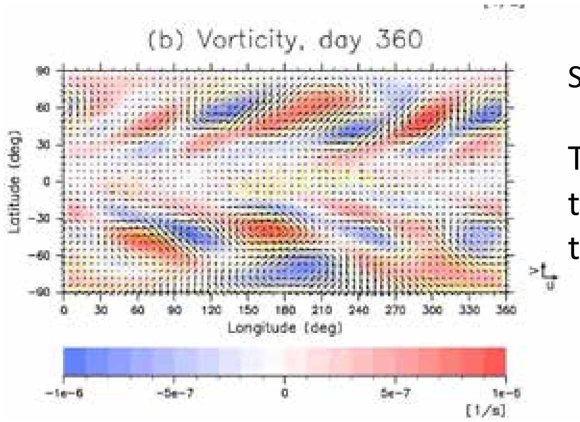

Sugimoto et al. (2014)

The superrotation of the atmosphere takes the place of planetary rotation, thereby sustaining baroclinic instability

$\langle u'v' \rangle$

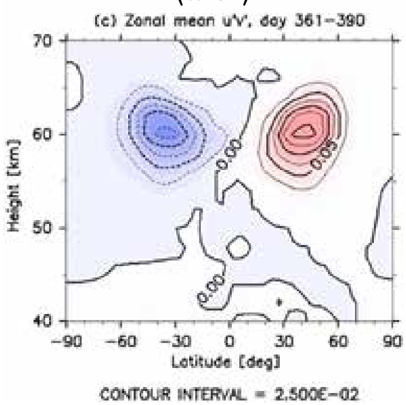

$\langle v'T' \rangle$

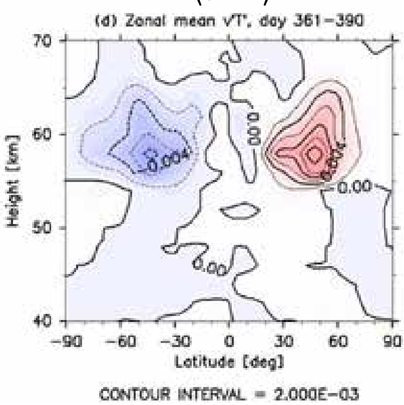

2.26 μm image of Venusian nightside taken by Akatsuki IR2

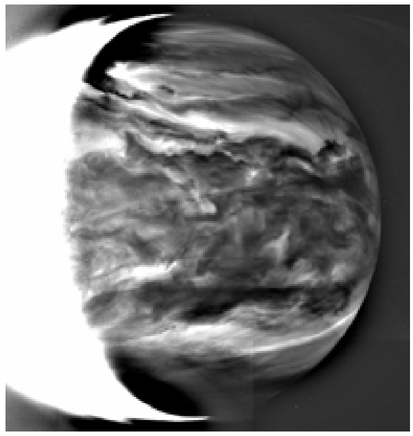

Wave momentum transport

baroclinic instability

→ generation of Rossby waves

→Rossby waves take away retrograde (westward) angular momentum from the md-latitude

→ maintenance of (eastward) mid-latitude jets

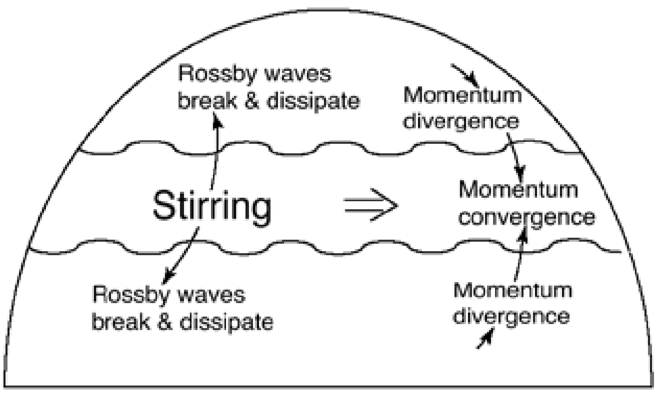

(Vallis, 2005)

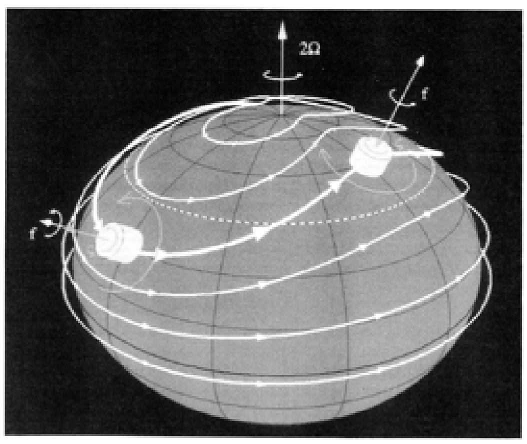

(Salby, 1996)

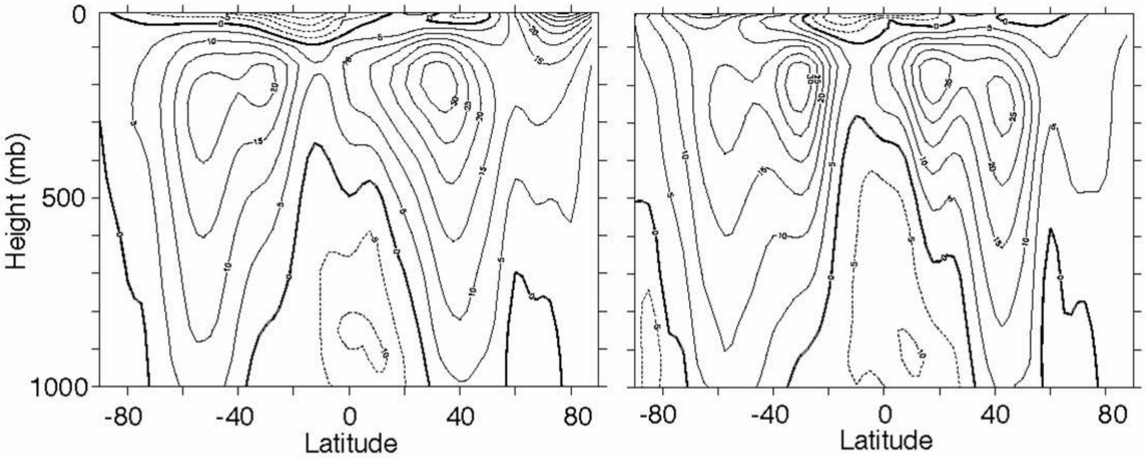

Fig. 3.1 The time-averaged zonal wind at 150°W (in the mid Pacific) in December-January February (DFJ, left), March-April-May (MAM, right). The contour interval is $5\,\mathrm{m\,s^{-1}}$. Note the double jet in each hemisphere, one in the subtropics and one in midlatitudes. The subtropical jets is associated with strong meridional temperature gradient, whereas the midlatitude jets have a stronger barotropic component and are associated with westerly winds at the surface.

Vallis (2006)

Latitudinal structures

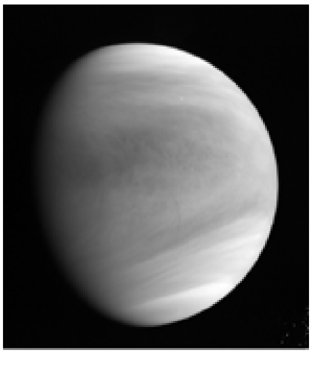

Rotation period	243 days	1 day	10 hours

Rossby radius of deformation

$$L_R = \frac{\sqrt{gH}}{f}$$

g : gravitational acceleration
H : depth of the system
$f = 2\Omega \cos\theta$: Coriolis parameter

The characteristic scale at which the velocity field and the pressure field adjust with each other to maintain geostrophic flow

Faster planetary rotation leads to large f, and then shorter L_R

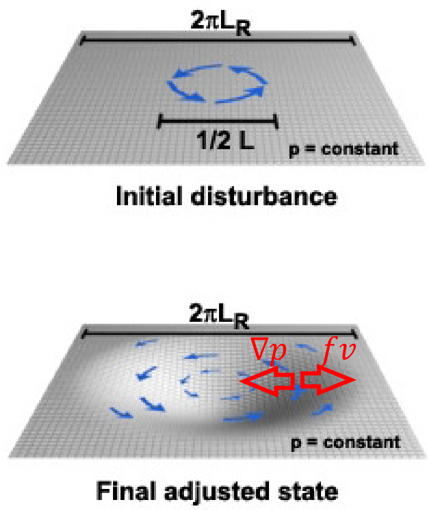

Parameter study of the atmospheric circulation of Earth-like planets with general circulation models (GCMs)

Williams (1988)

Zonal velocity

white : eastward

shade : westward

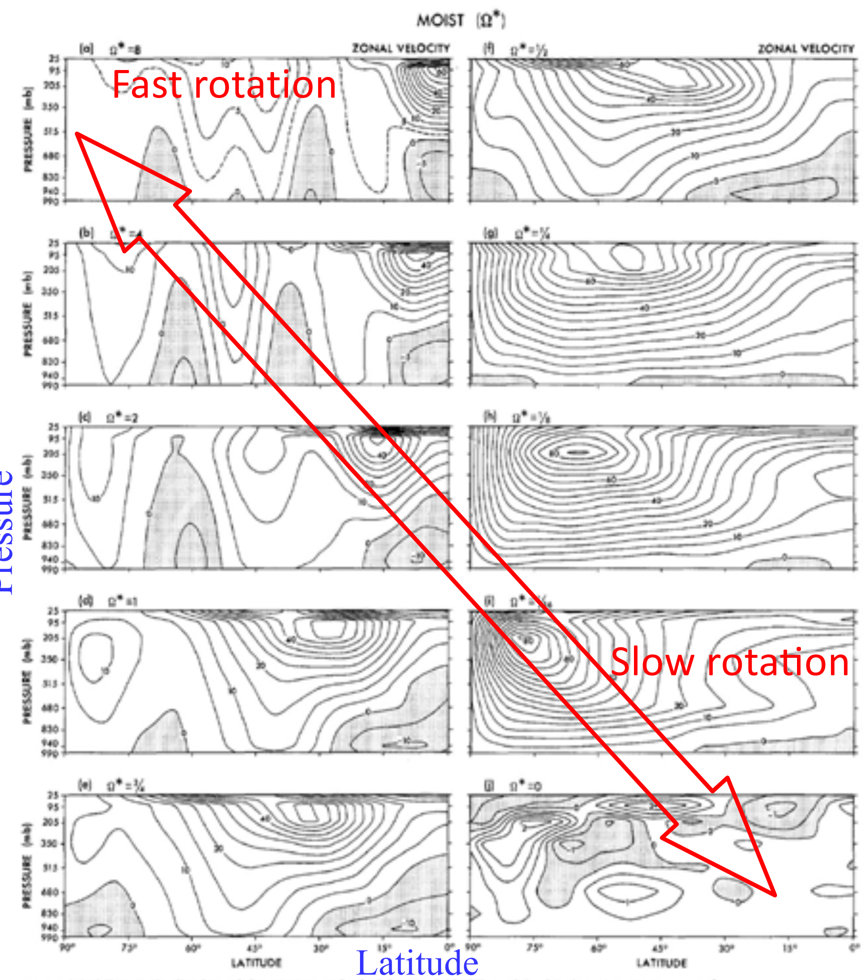

Fig. 2. Meridional distribution of the mean zonal wind for the MOIST model with Ω* = 0–8. Units: m s⁻¹

Meridional stream function

white : anti-clockwise

shade : clockwise

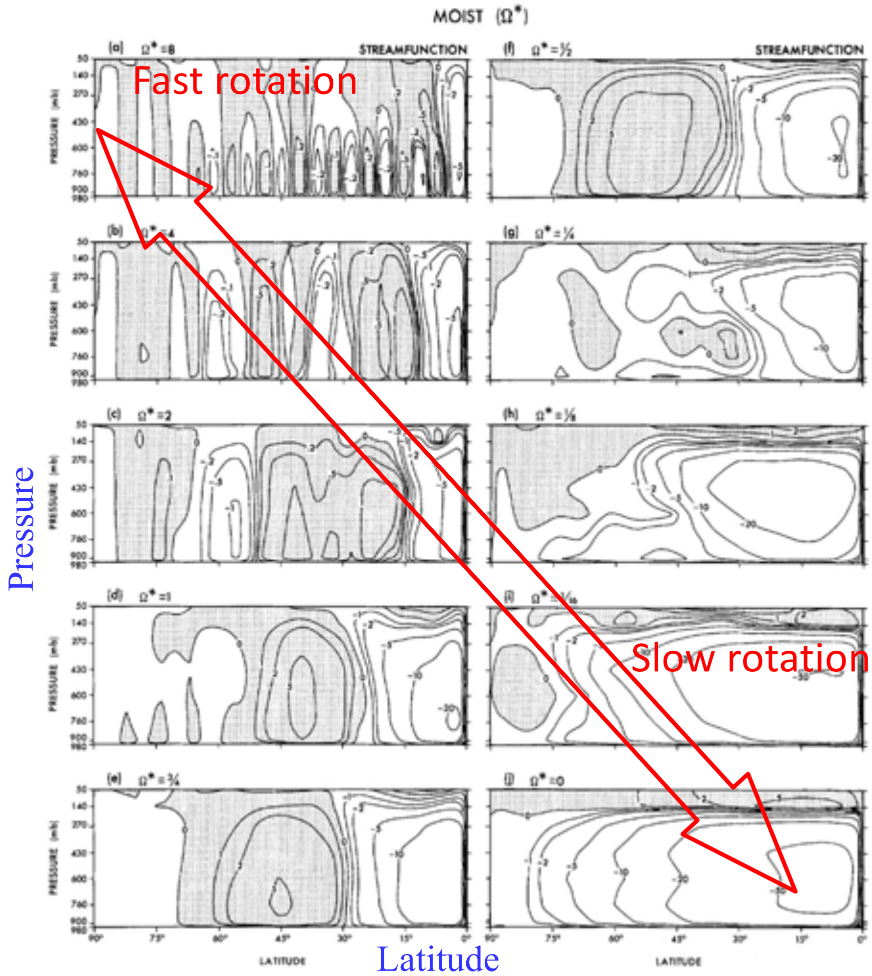

Fig. 3. Meridional distribution of the mean stream function for the MOIST model with $\Omega^* = 0$–8. Units: 10^{13} g s^{-1}

Temperature

white : > 220K

shade : < 220 K

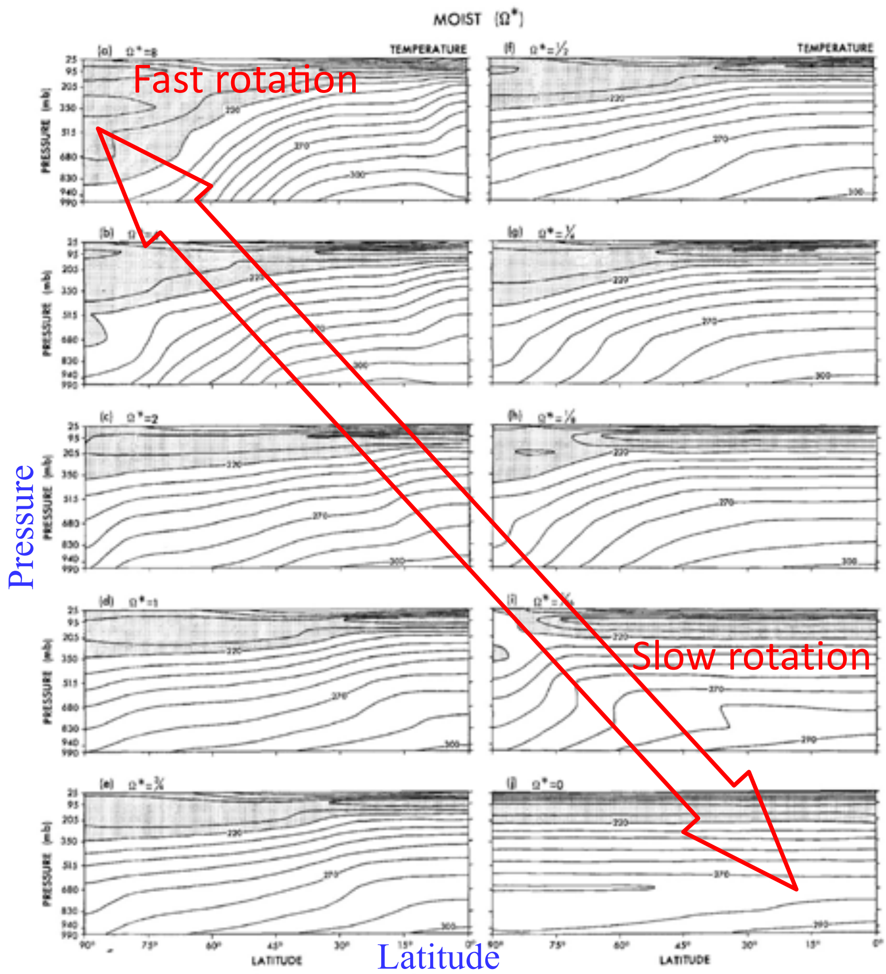

Fig. 4. Meridional distribution of the mean temperature for the MOIST model with $\Omega^* = 0$–8. Units: K

Superrotation

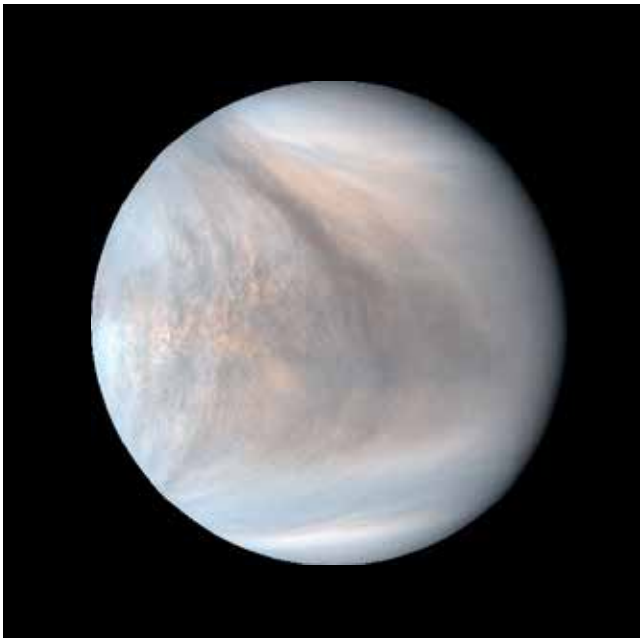

taken by Akatsuki UV Imager

Observed superrotating atmospheres

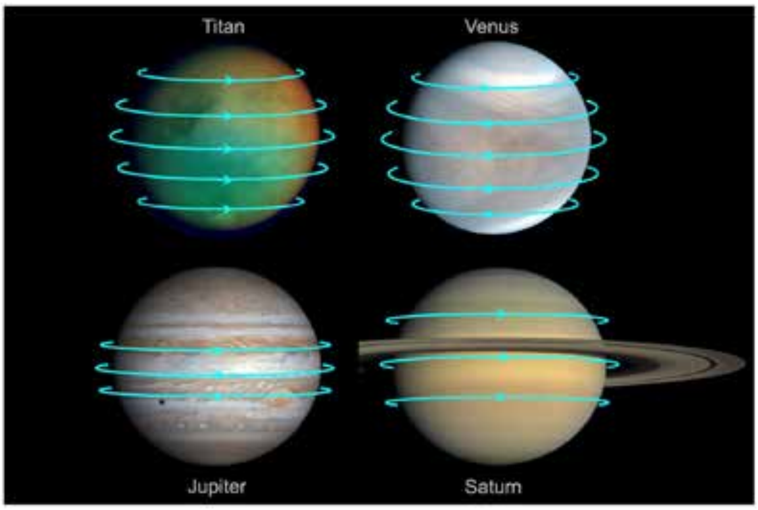

Planet	Radius (km)	Rotation period (days)	Equatorial rotation speed (m/s)	Equatorial wind speed (m/s)	Superrotation index, s, on the equator
Venus	6,052	243	1.81	100–120	55–66
Titan	2,576	16.0	11.7	100–180	8.5–15
Jupiter	69,911	0.41	12,300	60–140	0.005–0.011
Saturn	58,232	0.44	9,540	350–430	0.037–0.045
HD 189733b	79,500	2.2	2600	2400	0.92

Imamura et al. (2020, *Space Sci. Rev.*)

Superrotation of Venus’ atmosphere

Zonal winds measured by entry probes

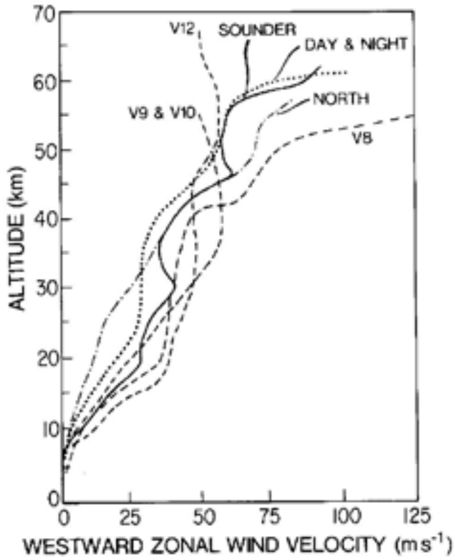

60 times faster rotation of the atmosphere (period=4 Earth days) than the solid planet (period=243 Earth days)

Superrotation of Venus’ atmosphere

Latitudinal profiles of the zonal wind speed at different levels (20–60 km) measured by entry probes

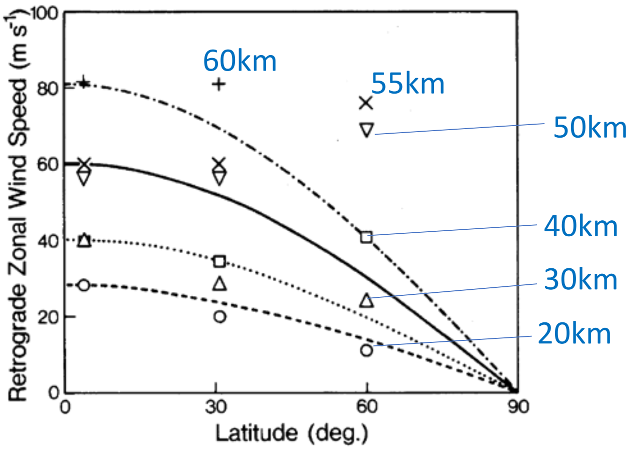

Fig. 10. Latitudinal variation of retrograde zonal wind speeds measured by interferometric tracking of Pioneer Venus probes. The symbols refer to different altitudes: 20 km, (0); 30 km, (Δ); 40 km, (□); 50 km, (▽); 55 km, (×); and 60 km, (+). The curves represent solid body rotation at different rates. It is assumed that the zonal circulation is approximately symmetric about the equator, so the wind speeds for the Day and Night probes can be plotted at 31°N.

Cloud-tracked winds from various missions

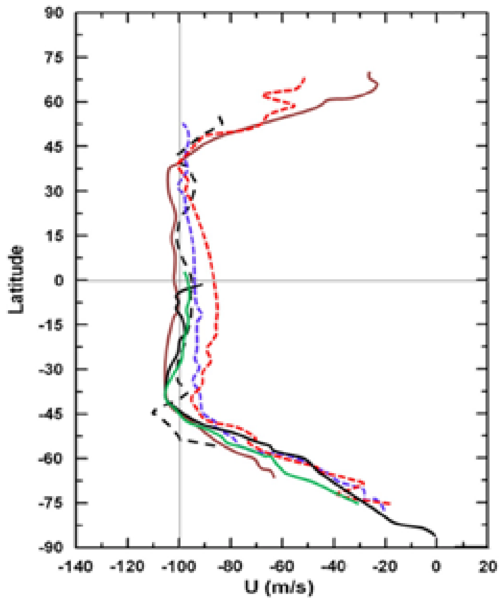

Sánchez-Lavega et al. (2017)

Superrotation of Titan' atmosphere

Hörst et al. 2017

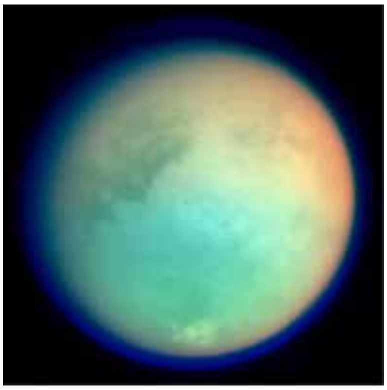

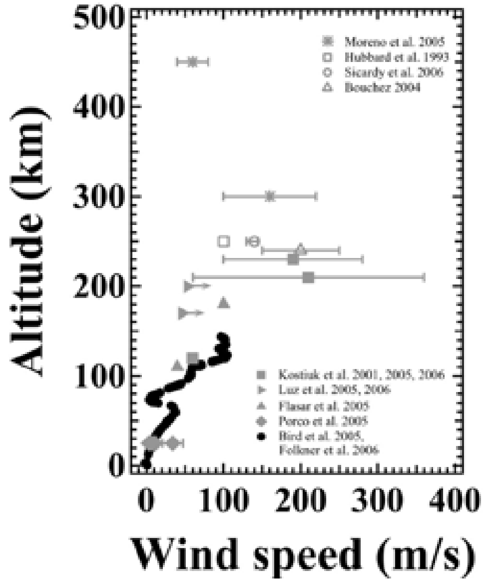

The atmosphere circulates 10 times faster than the rotation of the solid planet.

Infrared observation by CIRS on NASA Cassini

(northern winter)

Achterberg et al. 2008

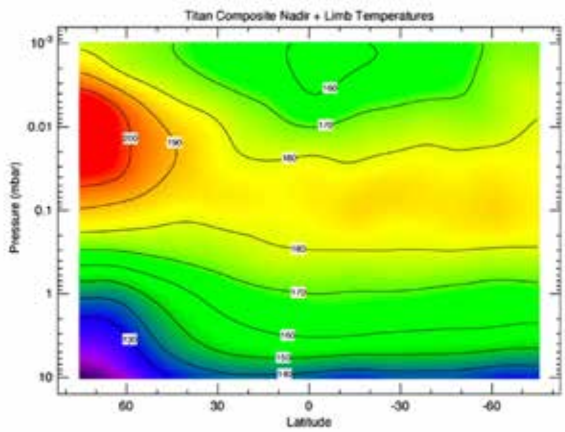

Zonal-mean temperature

Fig. 9. Zonal mean temperatures from all limb and nadir maps. Retrieved temperatures were averaged in 5° latitude bins, then smoothed with a 10° boxcar function applied three times. Contours are labeled in K.

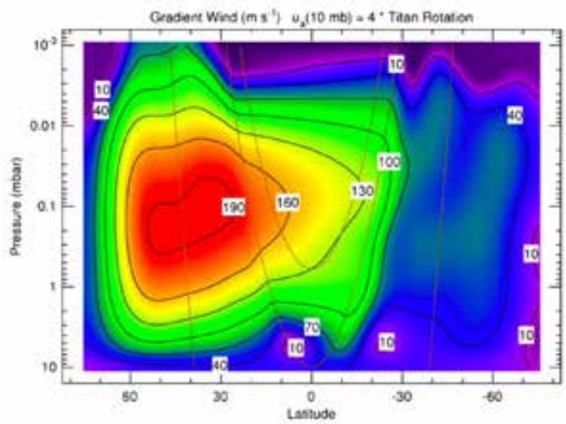

Zonal winds calculated from the temperature using thermal wind relation

Fig. 10. Zonal winds calculated from the temperatures in Fig. 9 from the gradient wind equation, assuming solid-body rotation at the 10 mbar level at four times Titan's rotation rate. Wind speed contours (black lines) are labeled in $m\,s^{-1}$. The gray lines indicate cylindrical surfaces parallel to the rotation axis along which the gradient wind equation is integrated. Equatorward and above the gray line tangent to the equator at 10 mbar, the winds are unconstrained by the gradient wind equation, and have been linearly interpolated on constant pressure surfaces.

Hide’s theorem

Hide (1969) showed that non-axisymmetric eddies (waves) are needed to maintain the jets aloft the surface and that the required momentum convergence should be provided by upgradient angular momentum transport.

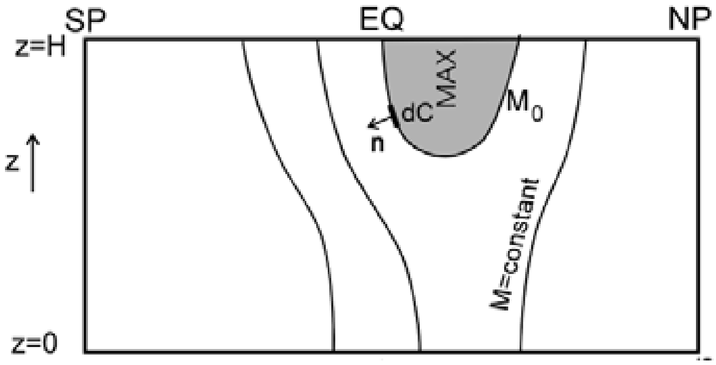

(Vallis, 2005)

$$R_o \equiv \frac{U}{fL}$$

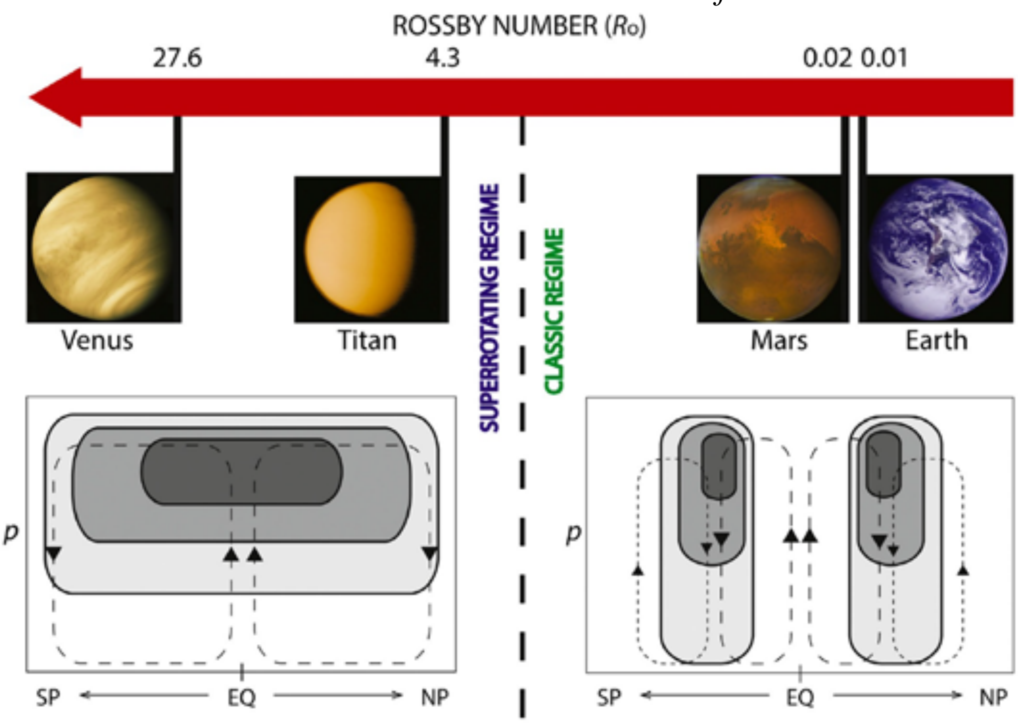

Fig. 1. Schematic view of the different Rossby numbers (R_0) and circulation regimes found on the terrestrial bodies of the Solar System with substantial atmospheres. R_0 was computed based on typical scales of zonal winds (around 100 m s^{-1} for Venus and Titan and 10 m s^{-1} for Earth and Mars), rotation rate, and planetary radius. The lower panels depicts a hypothetical vertical cross section of zonal mean zonal wind (shaded, arbitrary scale) and mean overturning circulation (dashed lines, arbitrary scales) characteristic of each body's atmospheres. See text for more details (photo credits: NASA/JPL).

Dias Pinto & Mitchell (2014)

password
eryeWKCF

Hypothesis: Acceleration by Hadley circulation and horizontal eddies（Gierasch, 1974; Rossow & Williams, 1979）

Hadley circulation

transports angular momentum poleward, thereby creating high-latitude jets.

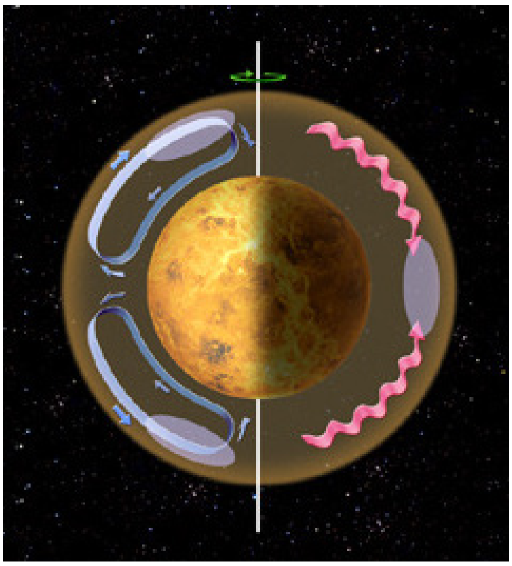

Horizontal eddies

transport angular momentum equatorward to smooth out the differential rotation of the atmosphere.

The combination of the two processes leads to an accumulation of angular momentum in the equatorial upper atmosphere.

Difference in wave characteristics between Earth and Venus

	Earth	Venus
		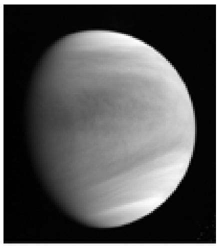
Rotation period	1 day	243 days
	Small waves	Large waves
	Poleward AM transport	?

Rossby radius of deformation: $L_R = \frac{\sqrt{gH}}{f}$

Rossby-Kelvin instability

(Sakai 1989; Iga and Matsuda 2005; Wang & Mitchell 2014)

Coupled mode seen in a Titan-like GCM (Wang & Mitchell 2014)

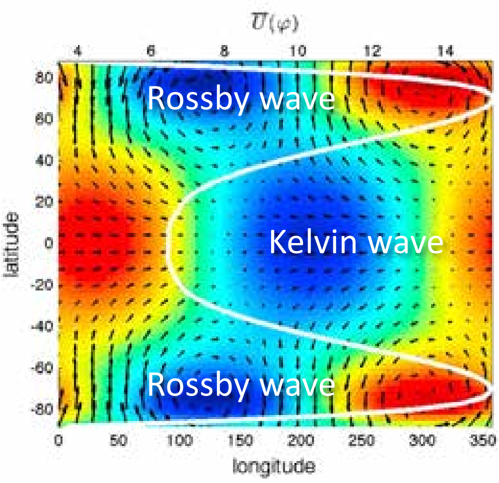

Coupled mode seen in a Venus GCM (Takagi et al. 2022)

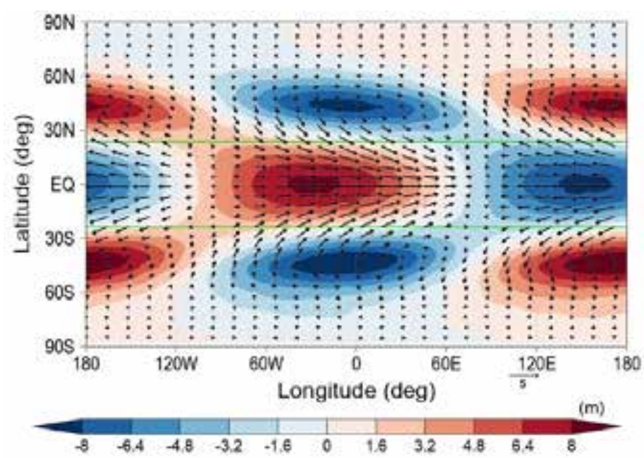

Planetary-scale shear instability can transport angular momentum equatorward

Parameter dependence in Earth-like GCM (Dias Pinto & Mitchell 2014)

Zonal velocity

Meridional circulation
Temperature

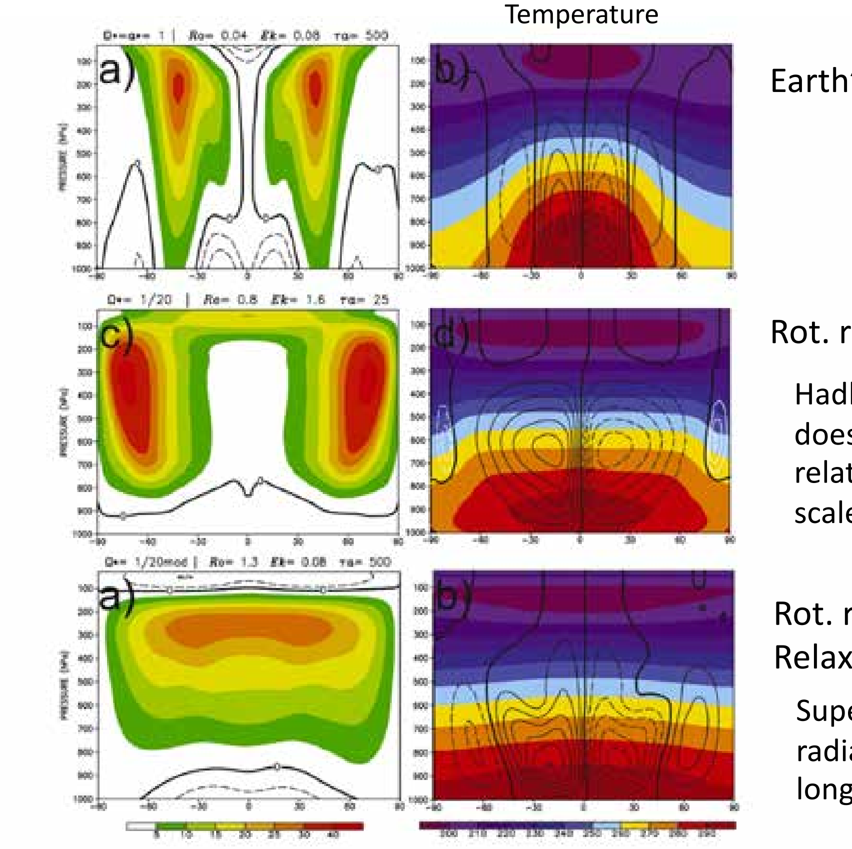

Earth' condition R_o = 0.04

Rot. rate x 1/20 R_o = 0.8

Hadley cell spreads, but superrotation does not develop because of the relatively short radiative/viscos time scale.

Rot. rate x 1/20 R_o = 1.2
Relaxation time x 20

Superrotation develops when the radiative/viscos time scales are made longer.

Radiative relaxation time

- The time scale over which the atmosphere is warmed by solar radiation or cooled by emitting infrared radiation.
- It is considered that the meridional circulation is determined by this time scale.

- The larger the heat capacity of the atmosphere, the longer the radiative relaxation time.
  - Mars

    Surface pressure = 0.006 bar → Relaxation time ~ 3 Earth days
  - Earth

    Surface pressure = 1 bar → Relaxation time ~ 100 Earth days
  - Venus

    Surface pressure = 92 bar → Relaxation time ~ 50 Earth years

Conditions for superrotation

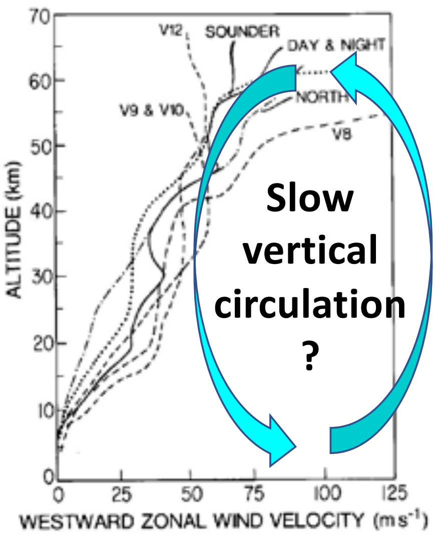

✓ Slow planetary rotation

- On slow-rotating planets, atmospheric waves caused by planetary-scale dynamical instabilities unknown in Earth's meteorology lead to an acceleration of the atmosphere. (When the planet rotates rapidly, atmospheric waves accelerate the atmosphere at high latitudes like the Earth)

✓ Long radiative relaxation time

- A dense atmosphere has a large heat capacity and a longer relaxation time. The vertical circulation slows down, making it difficult to smooth out the velocity change with altitude and making it easier to maintain the superrotation.

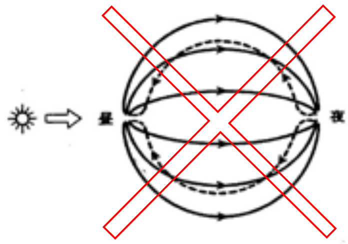

Another mechanism: Acceleration by thermal tides

(Fels & Lindzen 1974)

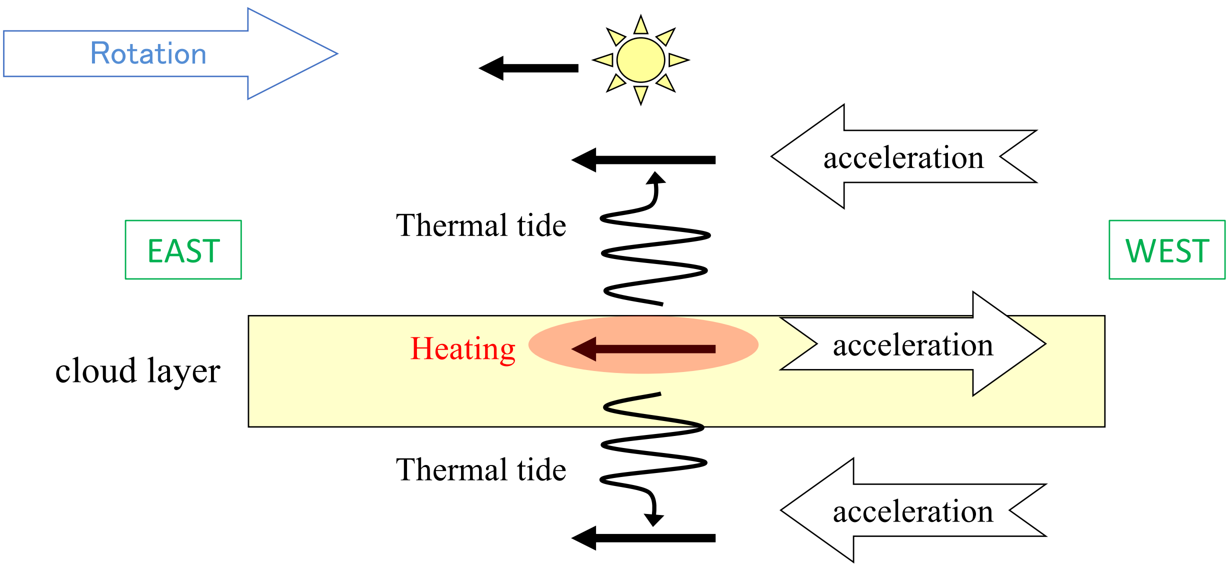

Eastward movement of the solar heating region in the cloud generates thermal tides (planetary-scale gravity wave) → The tides having eastward momentum propagate upward and downward → Vertical redistribution of momentum leads to a westward acceleration of the cloud-level atmosphere

Vertical structure of thermal tides in Venus's atmosphere

Linear solution (Takagi & Matsuda, 2006)

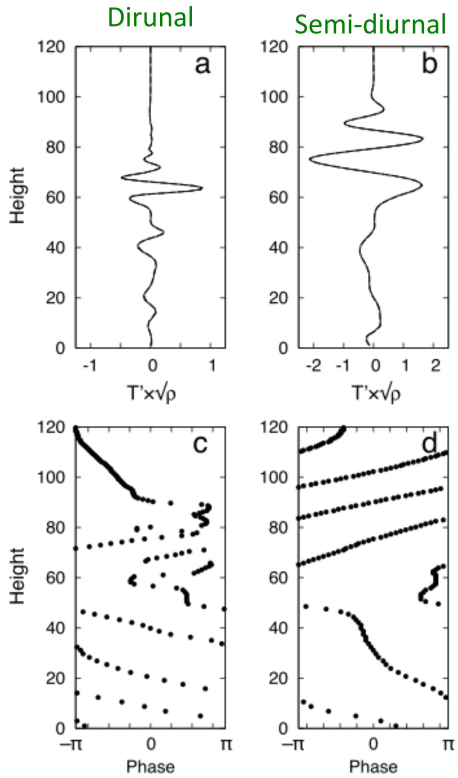

Temperature perturbation (Schofield & Taylor 1983)

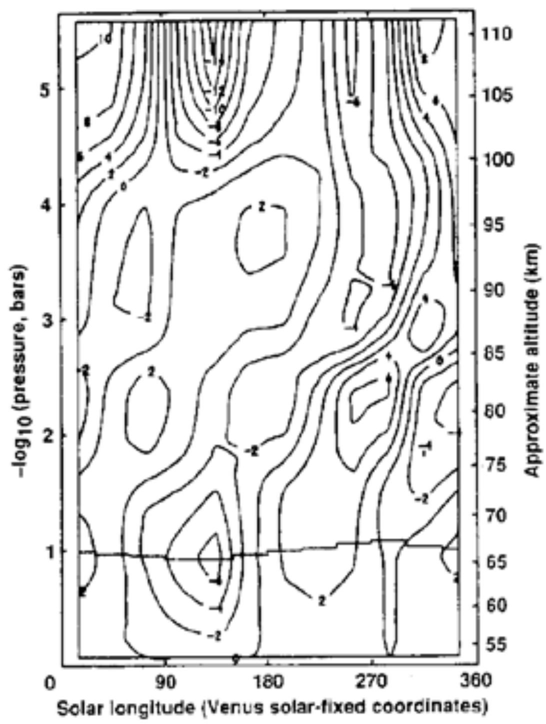

Wind field of thermal tides on Venus (Fukuya et al. 2021)

Clouds seen in thermal IR

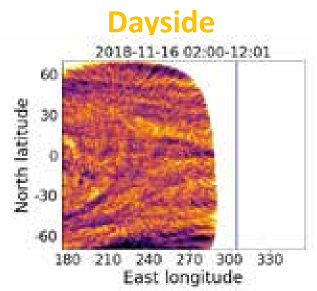

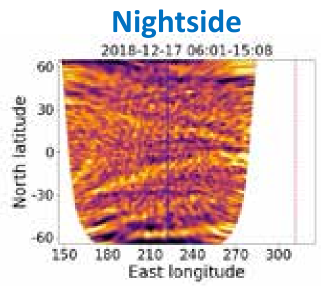

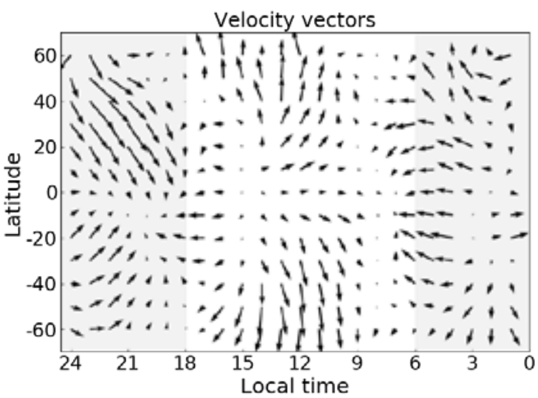

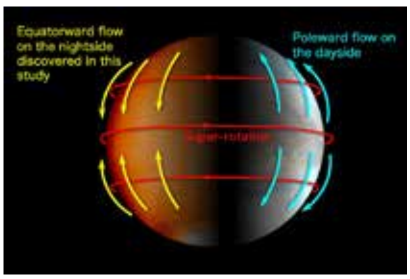

- Equatorward circulation was discovered on the nightside
- Dayside poleward flow and the nightside equatorward flow cancel each other

Numerical models of Venus

Zonal winds

Garate-Lopez and Lebonnois (2018)

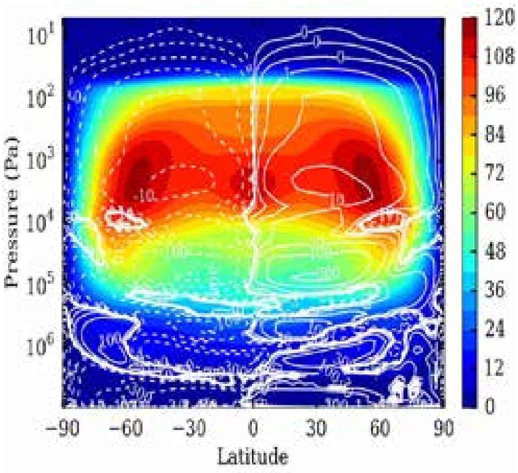

Sugimoto et al. (2014)

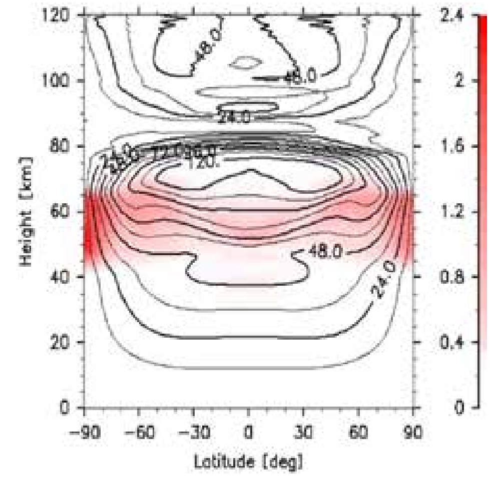

The Hadley circulation mechanism and the thermal tide mechanism seem to work simultaneously

Implications for exoplanets

- Tidally-locked planets are mostly slow rotators like Venus.
- Super-rotation can redistributes thermal energy along the local time on such planets.

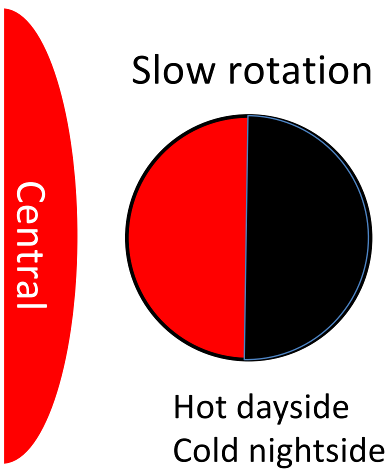

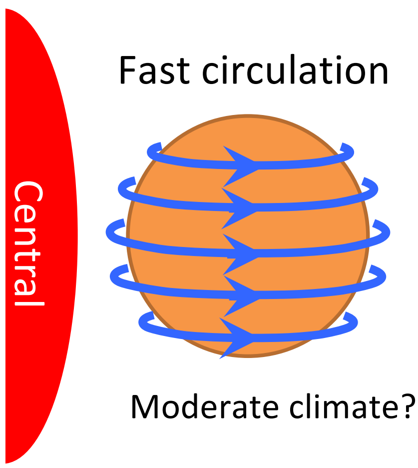

Antisolar

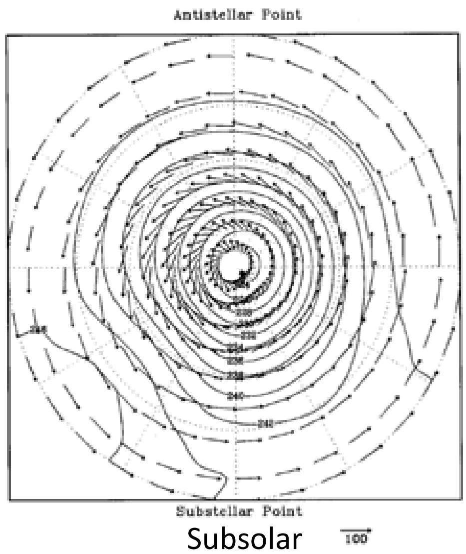

Subsolar

Polar view of the atmospheric circulation and temperature distribution at 20 km altitude on a synchronously rotating terrestrial planet (Joshi et al., 1997)

A map of the day-night contrast of the extrasolar planet HD 189733b (Knutson et al. 2007)

A minimum brightness temperature of 973 +/- 33 K and a maximum brightness temperature of 1212 +/- 11 K at a wavelength of 8 microns, indicating that energy from the irradiated dayside is efficiently redistributed throughout the atmosphere

Observed phase variation for HD 189733b, with transit and secondary eclipse visible.

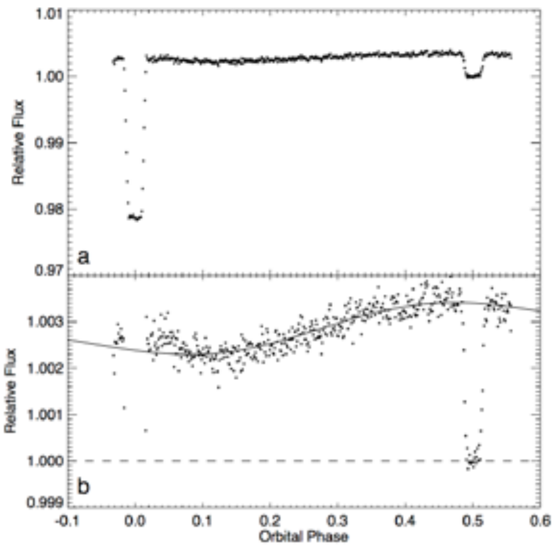

Brightness estimates for 12 longitudinal strips on the surface of the planet

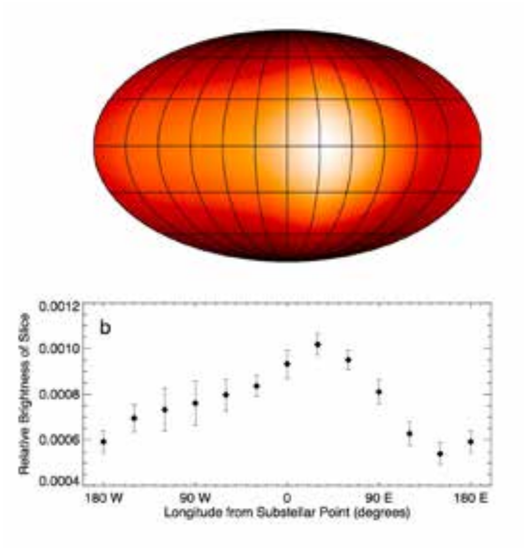

Linear, analytic solution for parameters relevant to hot, tidally locked exoplanets (Showman & Polvani 2011)

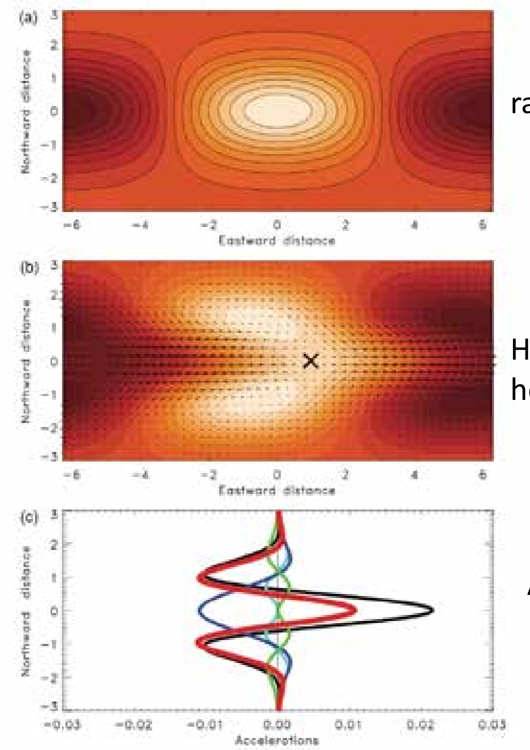

radiative-equilibrium height field

Height field (orange scale) and horizontal wind velocities (arrows)

Acceleration

Matsuno-Gill pattern (Matsuno 1966; Gill 1980)

- Heat-induced tropical circulation composed of Rossby wave and Kelvin wave
- Plays crucial roles in Earth's tropical troposphere

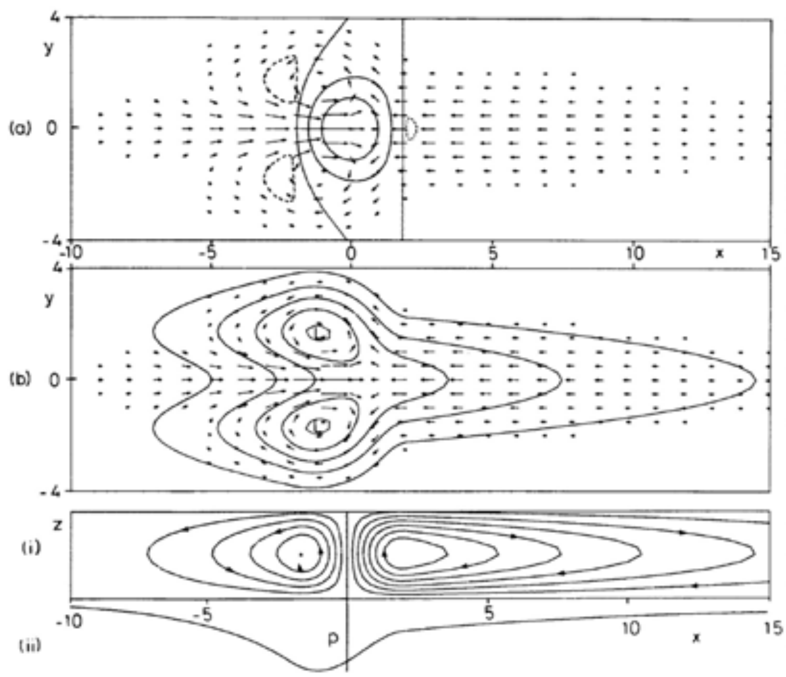

Figure 1. Solution for heating symmetric about the equator in the region $|x| < 2$ for decay factor $\epsilon = 0{\cdot}1$.
(a) Contours of vertical velocity w (solid contours are 0, 0·3, 0·6, broken contour is −0·1) superimposed on the velocity field for the lower layer. The field is dominated by the upward motion in the heating region where it has approximately the same shape as the heating function. Elsewhere there is subsidence with the same pattern as the pressure field.
(b) Contours of perturbation pressure p (contour interval 0·3) which is everywhere negative. There is a trough at the equator in the easterly régime to the east of the forcing region. On the other hand, the pressure in the westerlies to the west of the forcing region, though depressed, is high relative to its value off the equator.
Two cyclones are found on the north-west and south-west flanks of the forcing region.
(c) The meridionally integrated flow showing (i) stream function contours, and (ii) perturbation pressure. Note the rising motion in the heating region (where there is a trough) and subsidence elsewhere. The circulation in the right-hand (Walker) cell is five times that in each of the Hadley cells shown in (c).

Circulation of giant planet atmospheres

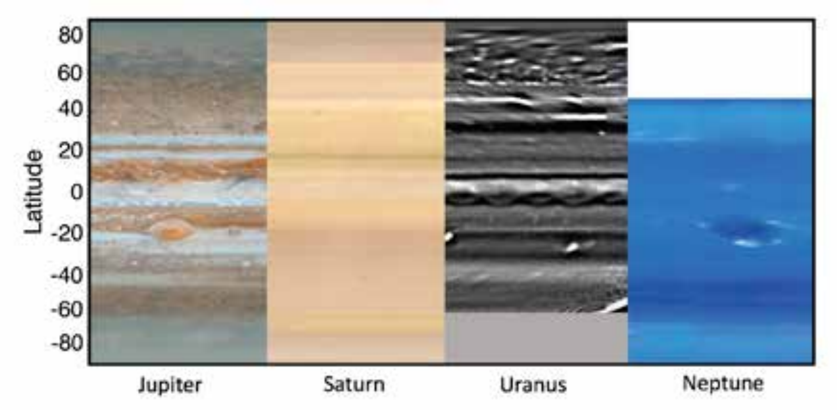

Fletcher et al. (2020, Space Sci. Rev.)

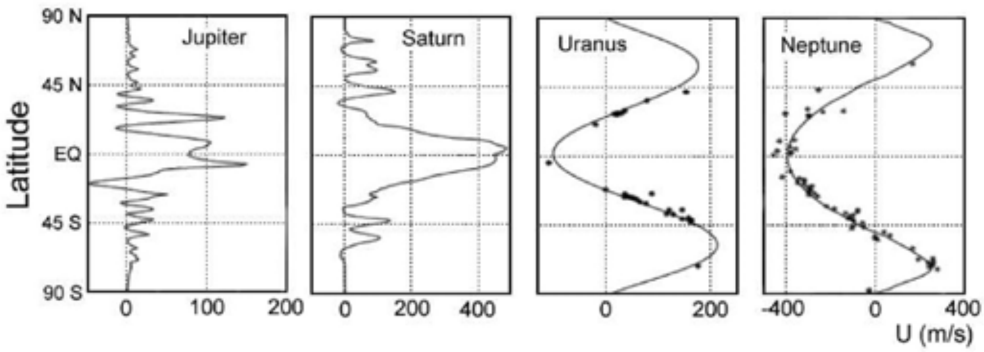

Sanchez-Lavega

Winds on Jupiter

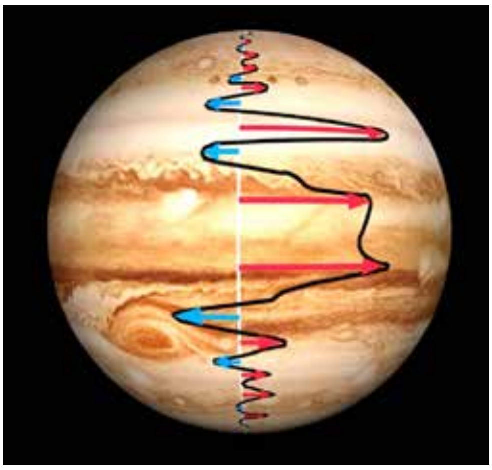

Zones :
- Reflective white bands of low temperatures, and elevated aerosol opacities
- Anti-cyclonic vorticity

Belts :
- Darker bands of warmer temperatures, and depleted aerosols
- Cyclonic vorticity

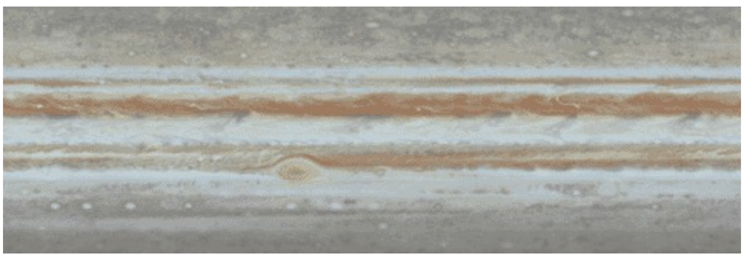

Cloud movie taken by Cassini spacecraft during its Jupiter flyby

Eddy momentum transport on Jupiter

Salyk et al. (2006)

Analysis of Cassini imaging data

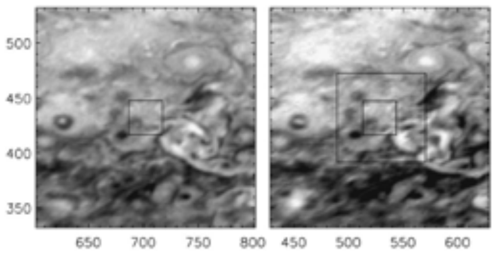

High positive correlation between eddy momentum flux, <u'v'>, and the variation of zonal velocity with latitude, du/dy, was found.

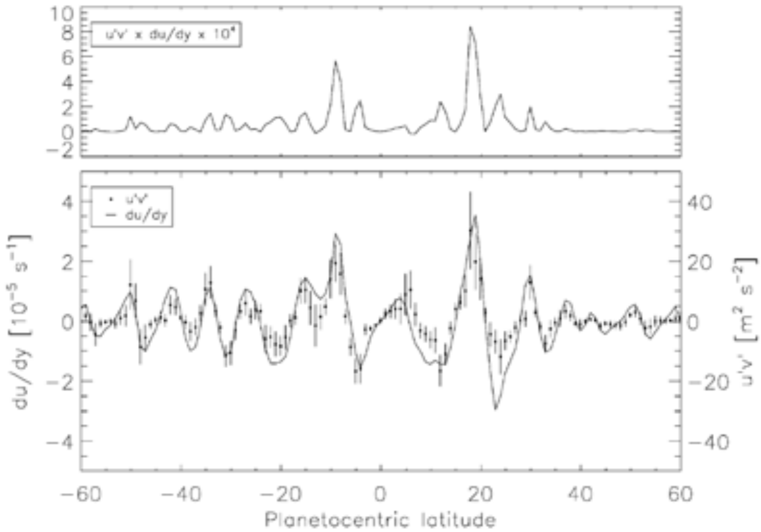

Thunderstorms on Jupiter

Becker et al. (2020)

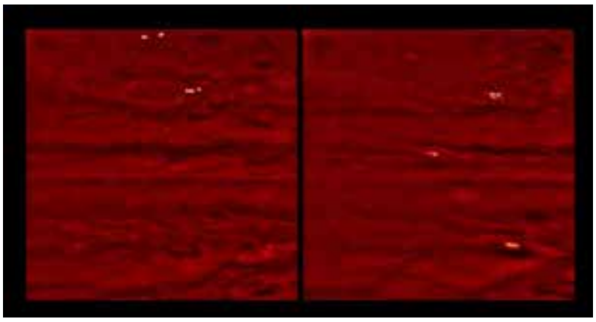

Lightning storms on the night side of Jupiter along with clouds dimly lit by moonlight from Io (taken by Galileo spacecraft)

On Jupiter, energy is transferred from the warm interior of the planet to the visible atmosphere to feed thunderstorms. Lightning occurs in the low-pressure regions.

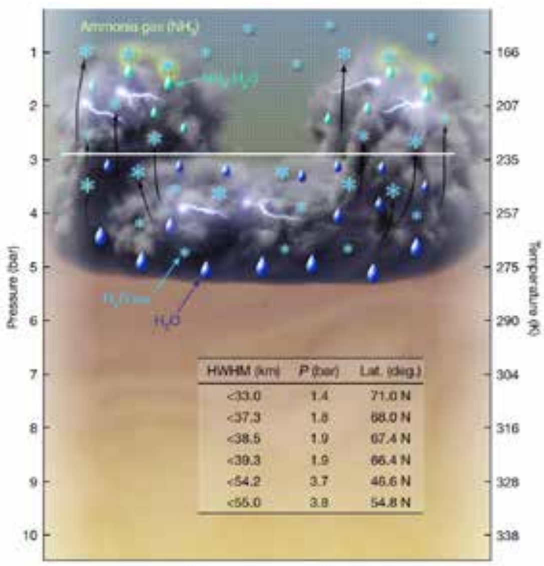

Fig. 3 | Conceptual illustration of lightning generation above and below the 3-bar level in Jupiter's atmosphere. Energetic updraughts (black arrows) loft water-ice particles to altitudes between 1.1 and 1.5 bar, where adsorption of ammonia gas onto ice particles melts the ice, creating falling liquid ammonia–water (NH_3–H_2O) particles (green drops). Charge separation occurs as the NH_3–H_2O particles collide with upward moving water-ice, followed by lightning. At pressures greater than about 3 bar, temperatures are above the limit for supercooled water (white line, about 233 K) and lightning is generated in pure water clouds. Inset, radial half-width at half-maximum (HWHM) intensity distances, estimated maximum depths of origin (*P*, pressure level) and latitudes (lat.) of observed SRU lightning flashes.

Superrotation on Jupiter and Saturn

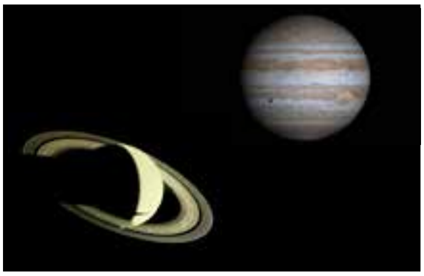

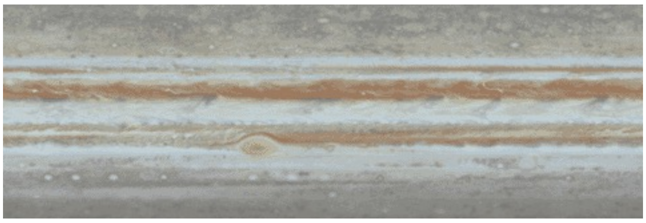

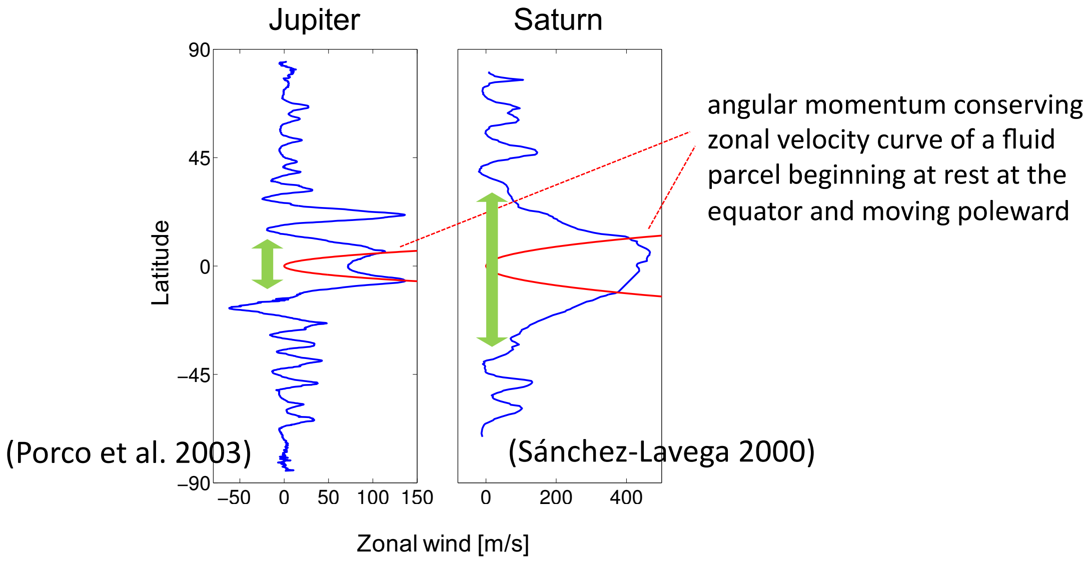

Modeling Jupiter and Saturn's zonal flows

- Shallow models
  - The dynamics are shallow, such as on a terrestrial planet
  - The strong east-west flows can result from 2D geostrophic turbulence and/or baroclinic instability

- Deep models
  - the observed jets are the surface manifestation of convective columns originating from the hot interiors

Two-dimensional turbulence

- Small eddies tend to organize large eddies as time passes
- Turbulent energy cascade toward large scales (smaller wavenumber *k*)

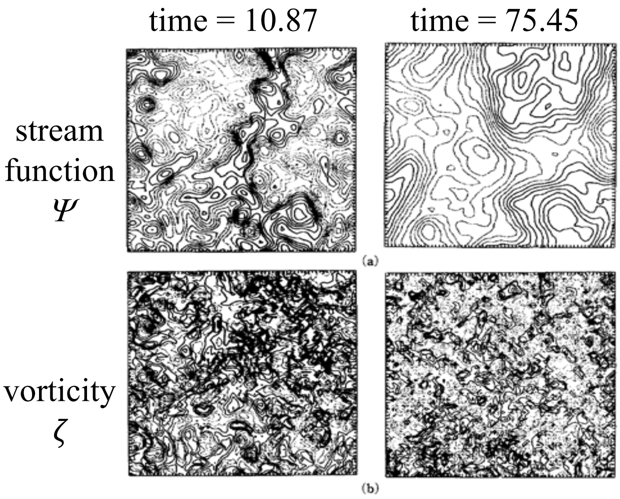

図 4.1 リリー（Lilly, 1969）の 2 次元乱流の数値実験の結果
左側の図が $t=10.87$，右側の図が $t=75.45$ での結果．(a)は流線関数，(b)は渦度の分布図．

Lilly (1969)

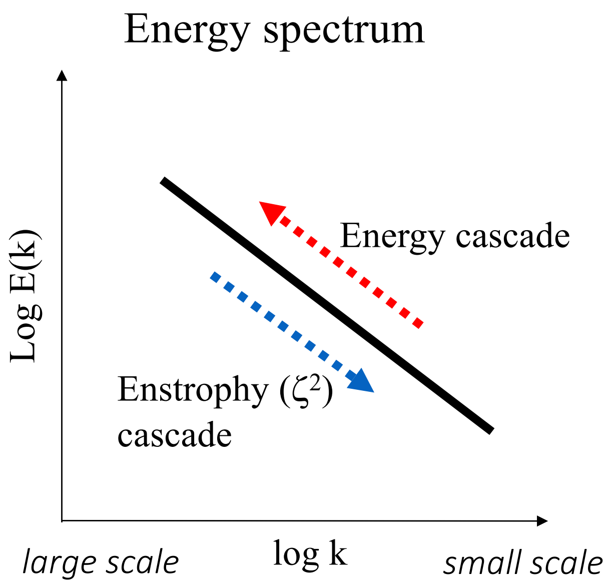

Rhines scale

- Vorticity equation

$$\left(\frac{\partial}{\partial t} + \vec{v}_g \cdot \nabla\right)(\zeta_g + f) = 0$$

linearization

$$\frac{\partial \zeta}{\partial t} + \underline{u\frac{\partial \zeta}{\partial x} + v\frac{\partial \zeta}{\partial v}} + \underline{\beta v} = 0$$

nonlinear term = origin of turbulence

beta effect = origin of Rossby wave

$k^2 U^2 > \beta U$: turbulence
$k^2 U^2 < \beta U$: Rossby wave

β : df/dy
U : typical velocity

- Rhines scale

$$k_\beta = \sqrt{\frac{\beta}{U}}$$

Upward cascade of turbulence energy stops at smaller scales ($k < k_\beta$)

→ This transition scale corresponds to the width of the jets.

Shallow-water turbulence on the sphere of the giant planets

- Forcing are given to the vorticity field as a small-scale, random process, or eddies are generated by baroclinic instability
- Inverse energy cascade generates multiple jets on the order of the Rhines scale
- The simulated equatorial flow is mostly retrograde

Zonal velocity

Scott & Polvani (2007)

Jupiter   Saturn   Uranus/Neptune

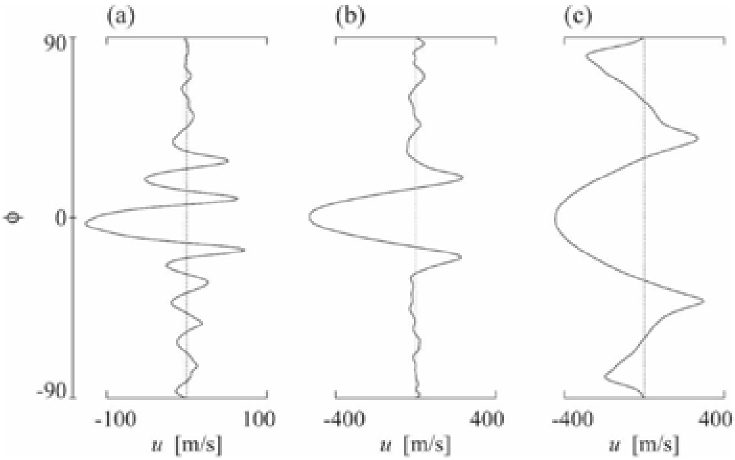

Vorticity field

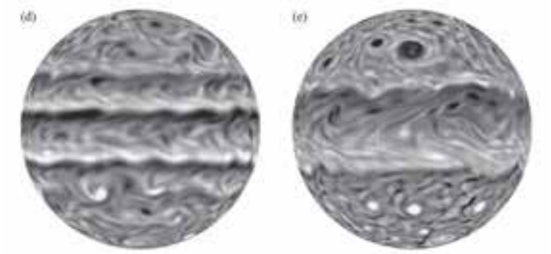

Jupiter (Ro=0.002)   Saturn (Ro= 0.013)

Deep models: Taylor–Proudman theorem

- In a fluid that is steadily rotated, the fluid velocity will be uniform along any line parallel to the axis of rotation.

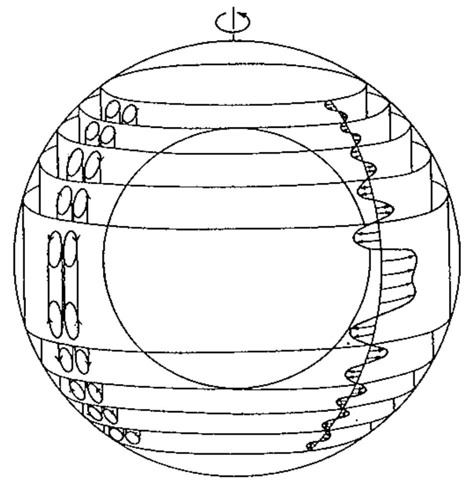

Busse (1994)

Momentum equation in rotational frame

$$\frac{d\vec{v}}{dt} + 2\vec{\Omega} \times \vec{v} + \frac{1}{\rho}\nabla p + \nabla\Phi = 0$$

Assuming non-compressivity and d/dt=0, the curl is applied to give

$$\vec{\Omega} \cdot \nabla\vec{v} = 0$$

Taking z-axis along the planet's rotational axis,

$$\frac{\partial \vec{v}}{\partial z} = 0$$

Thermal Rossby wave

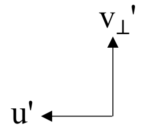

Reynolds stresses
$u'\,v_\perp' > 0$

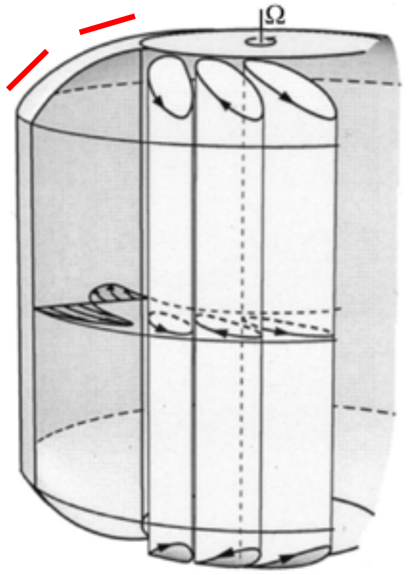

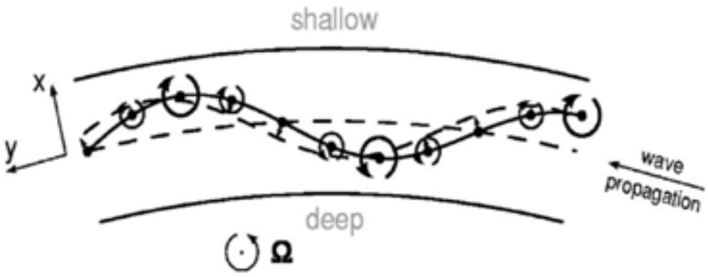

FIG. 2. The mechanism of propagation of a Rossby wave visualized in the equatorial plane of the rotating annulus: Fluid columns originally resting at the mid-surface acquire anticyclonic vorticity relative to the rotating system when they are displaced outwards towards the shallow region. Cyclonic vorticity is acquired by the displaced columns inwards. The action of the columnar motion on the neighboring fluid columns is such that an initial sinusoidal displacement propagates in the prograde direction.

Busse (2002)

The columns are tilted because the thermal Rossby wave has the tendency to propagate faster on the outside than on the inside. A prograde differential rotation on the outside with a retrograde one near the inner cylinder must thus be expected.

Quasi-geostrophic vorticity equation

$$\boxed{\frac{\partial \zeta_g}{\partial t} = -\vec{v}_g \cdot \nabla(\zeta_g + f) + f_0 \frac{\partial \omega}{\partial p}}$$

$$\zeta_g \equiv \frac{\partial v_g}{\partial x} - \frac{\partial u_g}{\partial y} = \frac{\nabla^2 \Phi'}{f_0}$$: geostrophic vorticity

Vorticity changes with time through

- advection of absolute vorticity ($\varsigma_g + f$) by geostrophic wind ($\vec{v}_g$)
- vertical divergence (horizontal divergence)

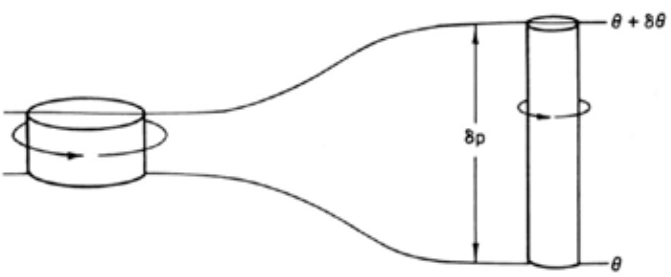

Holton (2004)

Fig. 4.7 A cylindrical column of air moving adiabatically, conserving potential vorticity.

Deep models

Observation Model Zonal velocity

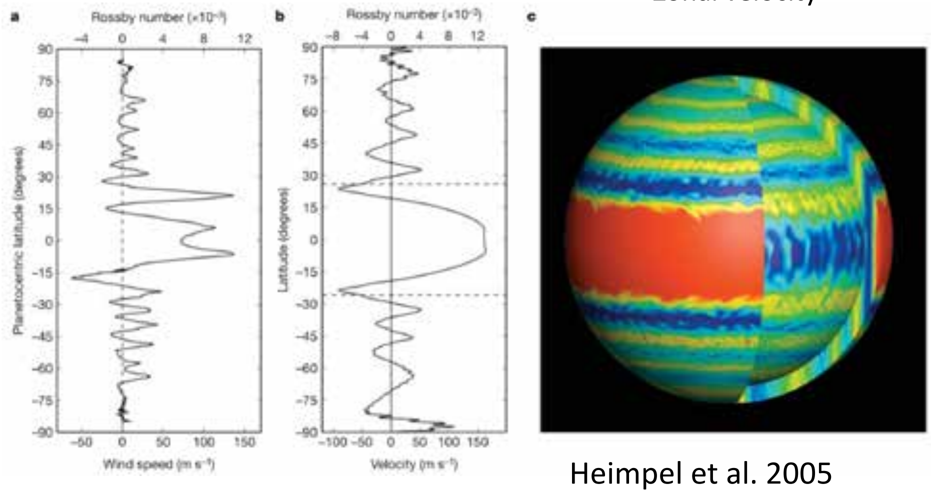

Heimpel et al. 2005

Showman et al. 2011

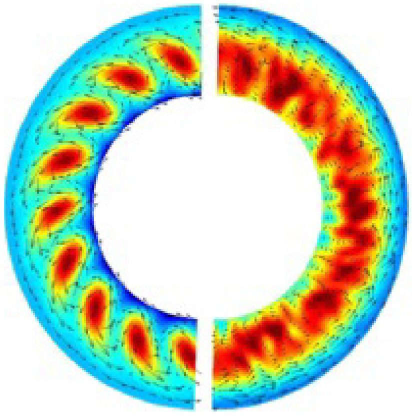

u'

$v_\perp'$

Reynolds stresses
$u'\, v_\perp' > 0$

Modeling of Jupiter

Schneider & Liu, 2009

baroclinic eddies generated by differential radiative heating are responsible for Jupiter's off-equatorial jets

zonal velocity

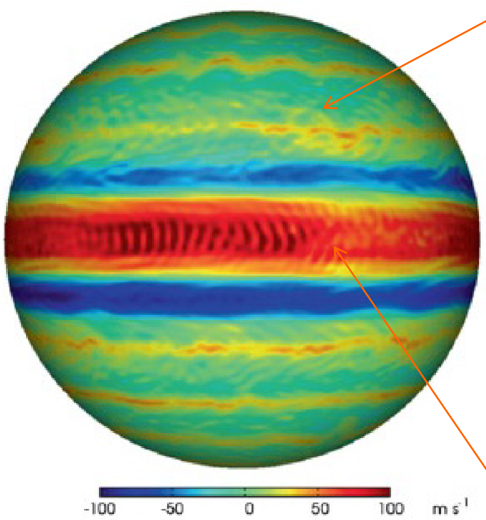

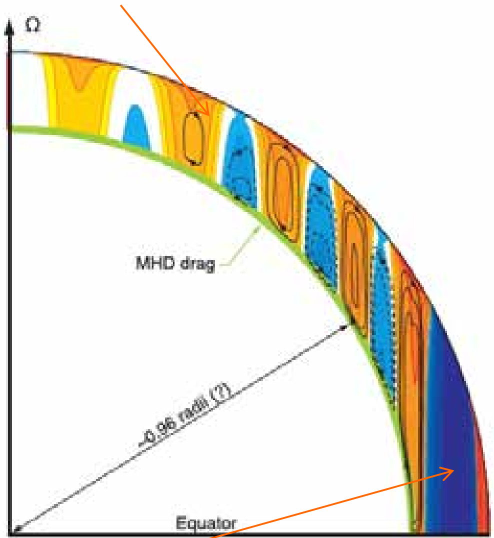

Rossby waves generated by intrinsic convective heat fluxes are responsible for the equatorial superrotation

Doppler tracking of Juno spacecraft

Less et al. (2018)

- The spacecraft acts as a test particle falling in the gravity field of the planet. Jupiter's gravity is inferred from range-rate measurements between a ground antenna and the spacecraft during perijove passes.
- The ground station transmits carrier signals, and the on-board translator lock the incoming carrier signals and retransmit them back to the ground. The range-rate (Doppler) observable is obtained by comparing the transmitted and received frequencies.
- Spherical harmonics representation of planetary gravity fields is determined by the density distribution inside the body.

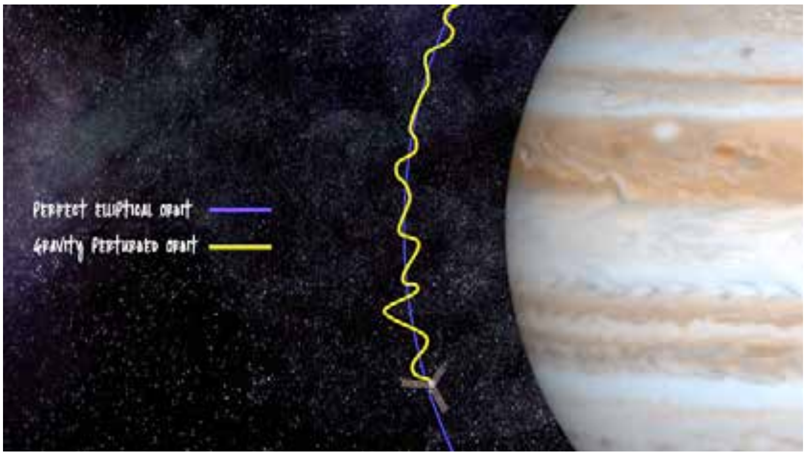

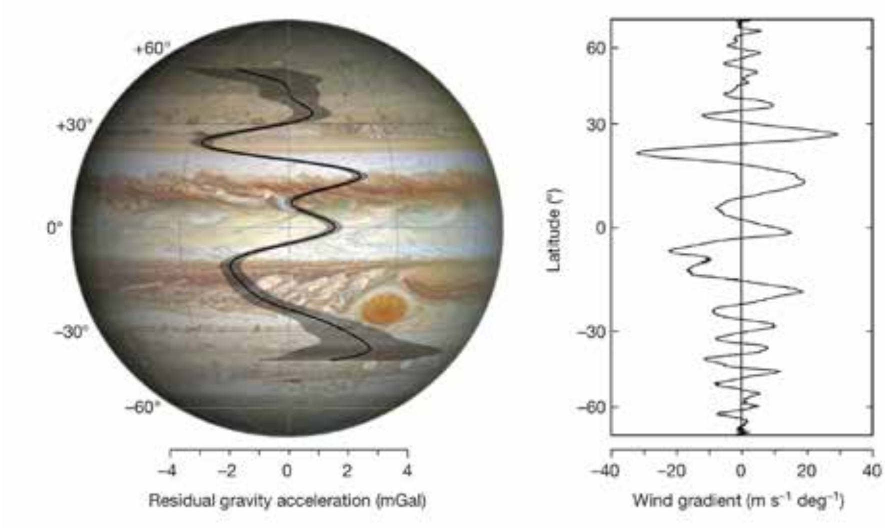

Figure 3 | Gravity disturbances due to atmospheric dynamics. a, An image of Jupiter taken by the Hubble Wide Field Camera in 2014 (https://en.wikipedia.org/wiki/Jupiter), showing the latitudinal dependence of residual gravity acceleration (in milligals, positive outwards) and associated 3σ uncertainty (shaded area) at a reference distance of 71,492 km, when the gravity from the even zonal harmonics J_2, J_4, J_6 and J_8 is removed. The residual gravity field, which is dominated by the dynamics of the flows, shows marked peaks correlated with the band structure. **b**, Latitudinal gradient of the measured wind profile. The largest (negative) peak of -3.4 ± 0.4 mGal (3σ) is found at a latitude of 24° N, where the latitudinal gradient of the wind speed reaches its largest value. The relation between the gravity disturbances and wind gradients is discussed in an accompanying paper[4].

Less et al. (2018)

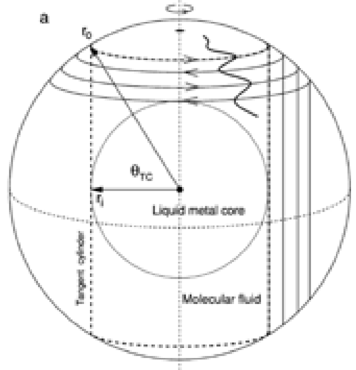

$$u(r,\theta) = u_{cyl}(s)Q(r) \tag{12}$$

where $u_{cyl}(s)$ is the cloud-level azimuthal wind projected downward along the direction of the axis of rotation, and $s = r\cos(\theta)$ is the distance from the axis of rotation. $Q(r)$ is the radial decay function we optimize, given by

$$Q(r) = (1-\alpha)\exp\left(\frac{r-a}{H(\theta)}\right) + \alpha\left[\frac{\tanh\left(-\frac{a-H(\theta)-r}{\Delta H}\right)+1}{\tanh\left(\frac{H(\theta)}{\Delta H}\right)+1}\right] \tag{13}$$

where a is the planetary radius, α is the contribution ratio between an exponential and a normalized hyperbolic tangent function and ΔH is the width of the hyperbolic tangent. We take a hierarchal approach using this profile at several levels of

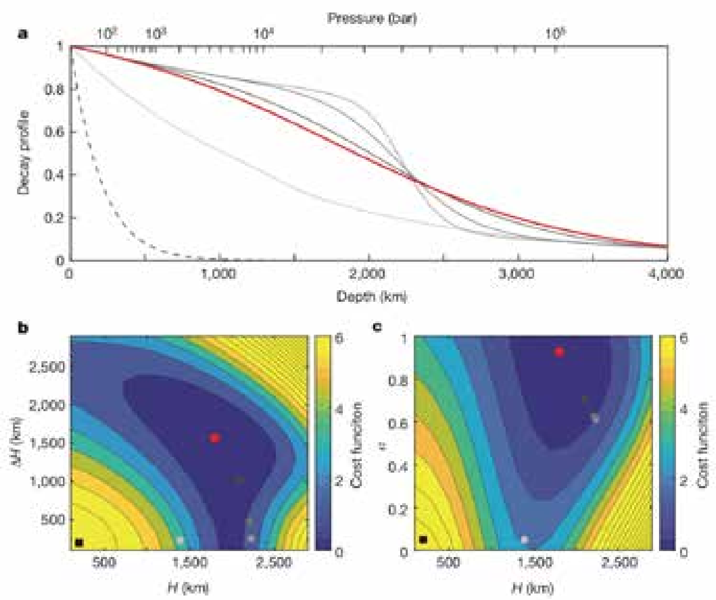

Kaspi et al. (2018)

The observed jet streams, as they appear at the cloud level, extend down to depths of thousands of kilometres beneath the cloud level, probably to the region of magnetic dissipation at a depth of about 3,000 kilometres

Difference between Jupiter and Saturn

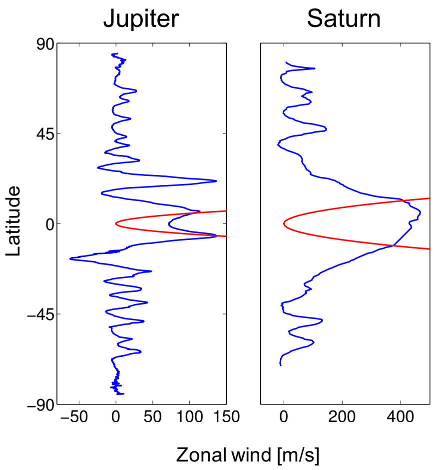

(Porco et al. 2003) (Sánchez-Lavega 2000)

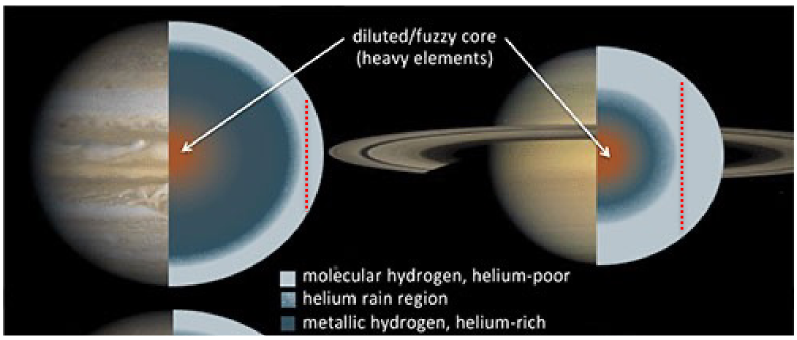

Helled (2019)

- According to gravity measurements by the Cassini spacecraft, Saturn's jets extend to about three times the depth of Jupiter's (Jupiter: 3000 km vs. Saturn: 9000 km). This is believed to correspond to depths where the atmosphere becomes conductive, causing Ohmic resistance.
- The latitudes at which equatorial super-rotation exists are <13° on Jupiter and <31° on Saturn. These transition latitudes correspond to where a line extended from the depth where conductivity occurs intersects the surface in the direction of the rotational axis.

Equatorial superrotation in the Sun

Rotation rates revealed by helioseismology

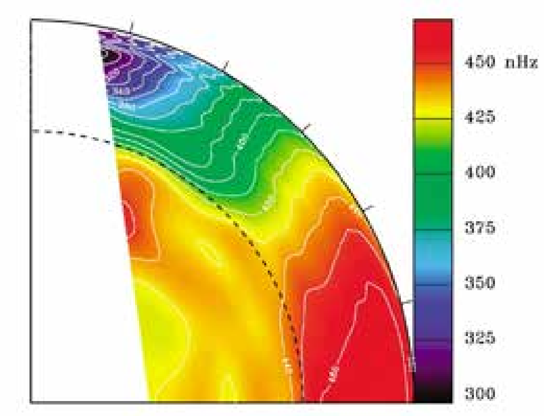

Rot. rate = 25 days on the equator

36 days near the poles

Numerical modeling (Miesch 2000)

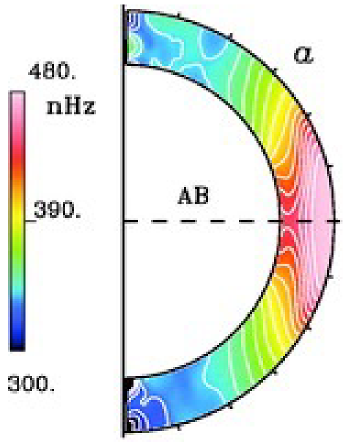

Vertical velocity at r = 0.95 $R_\odot$

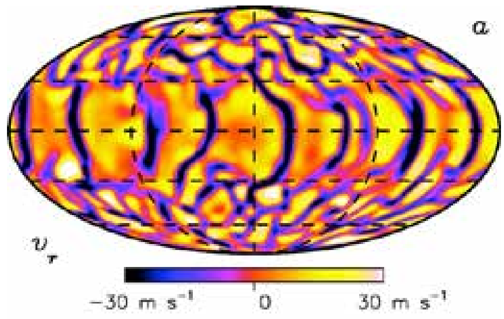

Equatorward angular momentum transport by slant convection ?

Driving forces of the meridional circulation

Transformed Eulerian-mean (TEM) equations:

Momentum eq.

$$\frac{\partial \bar{u}}{\partial t} + \boxed{\bar{v}^*}\left(\frac{\partial \bar{u}}{\partial y} - f\right) + \boxed{\bar{w}^*}\frac{\partial \bar{u}}{\partial z} = \boxed{\frac{1}{\rho_0}\left(\frac{\partial F^{(y)}}{\partial y} + \frac{\partial F^{(z)}}{\partial z}\right)}$$

zonal acceleration by waves

Residual mean meridional circulation
= Net Lagrangian transport

$$\bar{v}^* = \bar{v} - \frac{1}{\rho_0}\frac{\partial}{\partial z}\left(\rho_0 \frac{\overline{v'\theta'}}{\bar{\theta}_z}\right)$$

$$\bar{w}^* = \bar{w} + \frac{1}{\rho_0}\frac{\partial}{\partial y}\left(\frac{\overline{v'\theta'}}{\bar{\theta}_z}\right)$$

Eliassen-Palm flux (EP flux)

$$F^{(y)} = -\rho_0 \overline{u'v'}$$

$$F^{(z)} = -\rho_0\left(\overline{u'w'} - f\frac{\overline{v'\theta'}}{\bar{\theta}_z}\right)$$

Thermal energy eq.

$$\frac{\partial \bar{\theta}}{\partial t} + \boxed{\bar{v}^*}\frac{\partial \bar{\theta}}{\partial y} + \boxed{\bar{w}^*}\frac{\partial \bar{\theta}}{\partial z} = \boxed{\bar{Q}}$$

diabatic heating

木田秀次（1983）

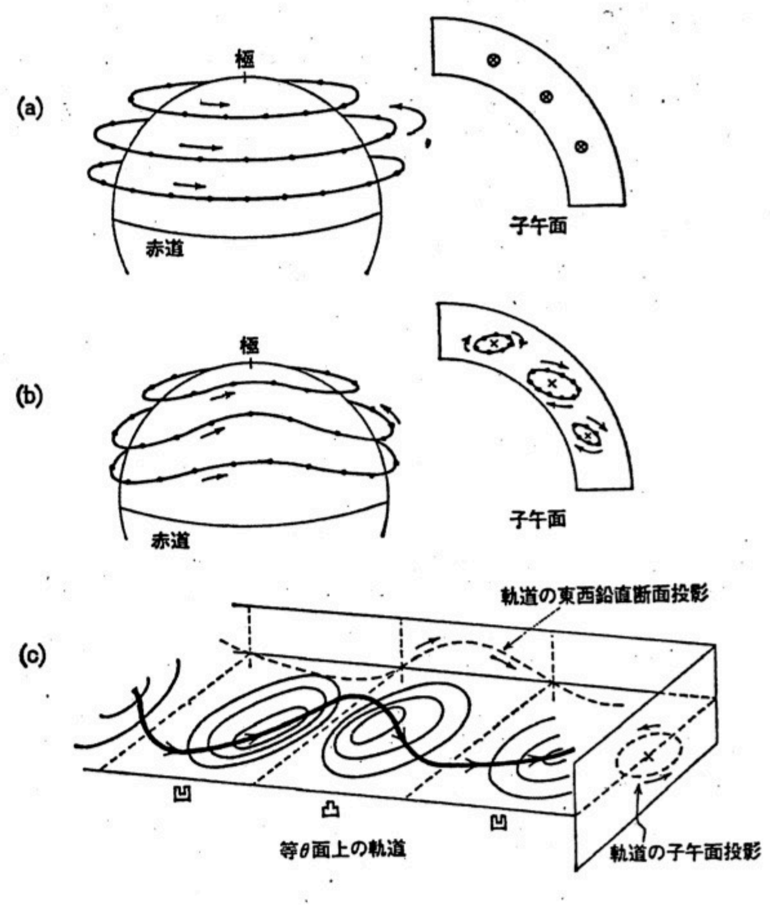

図 5.6 偏西風の中をプラネタリー波が鉛直伝播するときの空気塊の振動．小さい黒点は，微小空気塊を表わす．(a) 波が不在の場合．(b) 波が在る場合．× 印は子午面断面上の元の位置．(c) 等温位面上の空気塊の軌道．子午面投影では主軸が傾斜した楕円軌道になる．

Wave-driven meridional circulation

$$\cancel{\frac{\partial \bar{u}}{\partial t}} + \bar{v}^* \left(\cancel{\frac{\partial \bar{u}}{\partial y}} - f \right) + \bar{w}^* \cancel{\frac{\partial \bar{u}}{\partial z}} = \boxed{\frac{1}{\rho_0} \left(\frac{\partial F^{(y)}}{\partial y} + \frac{\partial F^{(z)}}{\partial z} \right)}$$ wave forcing

$$\therefore f \bar{v}^* = \boxed{\frac{1}{\rho_0} \left(\frac{\partial F^{(y)}}{\partial y} + \frac{\partial F^{(z)}}{\partial z} \right)}$$

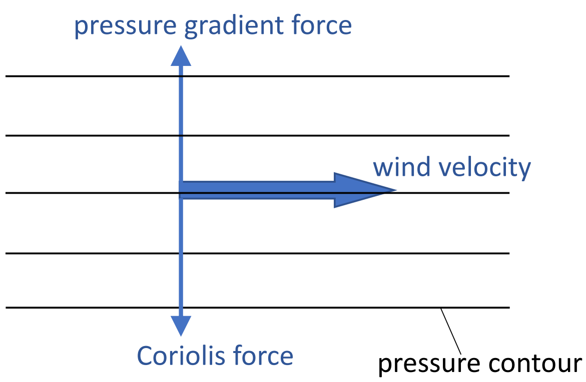

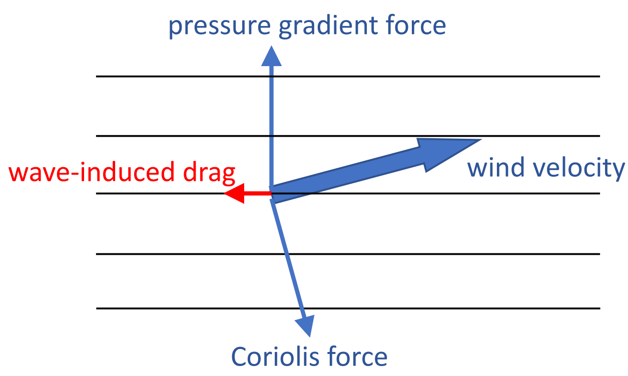

Earth's stratospheric meridional circulation (Holton 2012)

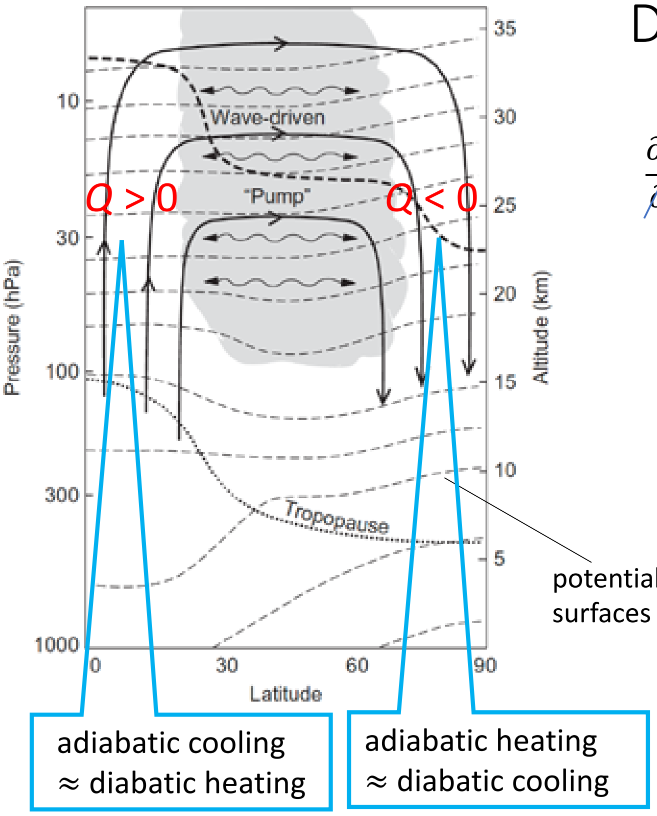

potential temperature surfaces

Diabatic circulation

$$\cancel{\frac{\partial\bar{\theta}}{\partial t}} + \bar{v}^* \cancel{\frac{\partial\bar{\theta}}{\partial y}} + \bar{w}^* \frac{\partial\bar{\theta}}{\partial z} = \bar{Q}$$

$$\boxed{\bar{w}^* \frac{\partial\bar{\theta}}{\partial z}} = \boxed{\bar{Q}}$$

adiabatic heating/cooling
断熱加熱

diabatic heating/cooling
非断熱加熱

Earth's mean meridional circulation in the troposphere

Holton 2004

Eulerian-mean

$(\bar{v}, \bar{w})$

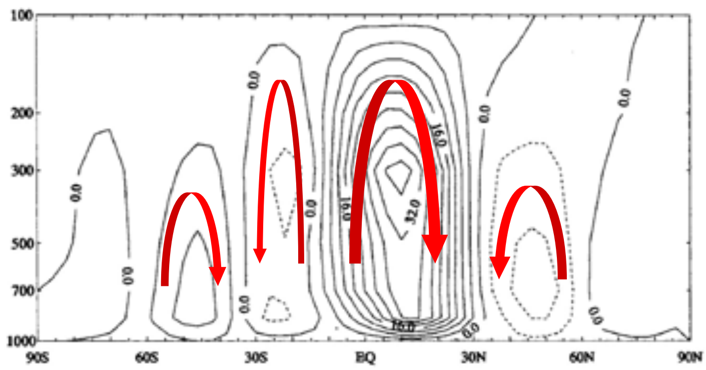

Fig. 10.7 Streamfunction (units: 10^2 kg m^{-1}s^{-1}) for the observed Eulerian mean meridional circulation for Northern Hemisphere winter, based on the data of Schubert et al. (1990).

Lagrangian-mean

$(\bar{v}^*, \bar{w}^*)$

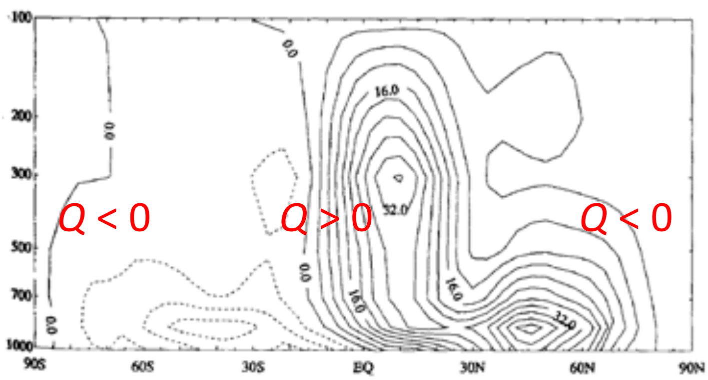

Meridional circulation of Mars atmosphere (Santee & Crisp 1995)

Mean temperature

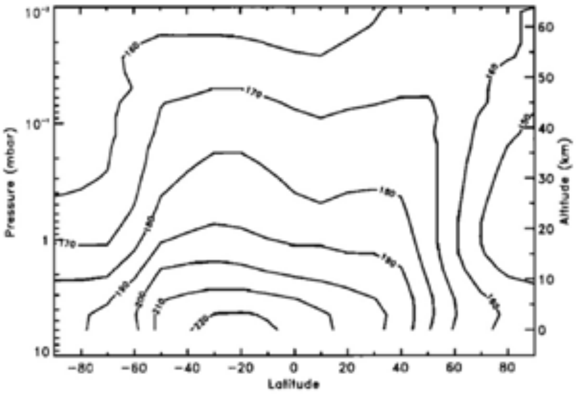

Figure 1a. Diurnal–mean temperatures obtained by averaging the 1400 LT and 0200 LT temperature maps retrieved from the Mariner 9 IRIS spectra in Paper I. For consistency with the results of Paper I, the vertical coordinate in this and all subsequent figures is the atmospheric pressure p. The approximate altitude z corresponding to a given pressure level is also included in these figures (see section 2.1). This correlation of altitude with pressure is based on the following values: $p_s = 6.0$ mbar, $R = 191.0$ J K^{-1} kg^{-1}, $g = 3.74$ m/s^2, and $T_0 = 196$ K (the globally and diurnally averaged value of the atmospheric temperature at the surface), resulting in a mean scale height $H = 10$ km.

Net radiative heating rate, Q

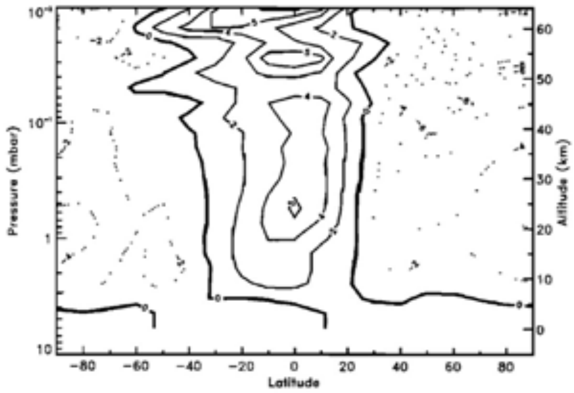

Figure 3. Net radiative heating rates (K/d) calculated from retrieved IRIS temperatures and dust abundances using the radiative transfer model described by *Crisp* [1990] and in the appendix of *Santee* [1993]. Negative contours are dashed, the zero contour is thicker, and the contour interval is nonuniform.

Meridional circulation of Mars atmosphere (Santee & Crisp 1995)

Meridional velocity $(\bar{v}^*)$

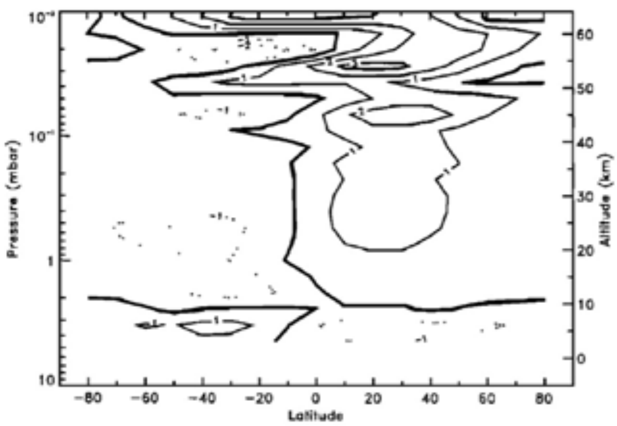

Figure 4a. Diabatic meridional velocity, in m/s. Positive values represent northward winds, negative contours are dashed, and the zero contour is thicker.

Vertical velocity $(\bar{w}^*)$

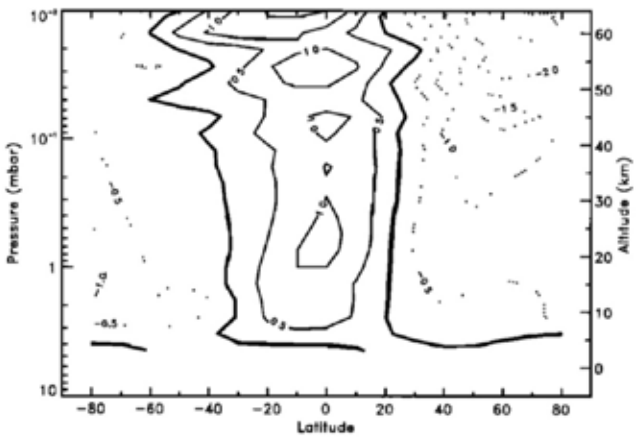

Figure 4b. Diabatic vertical velocity, in cm/s. Positive values represent upward winds, negative contours are dashed, and the zero contour is thicker.

Meridional circulation of Mars atmosphere (Santee & Crisp 1995)

Stream function

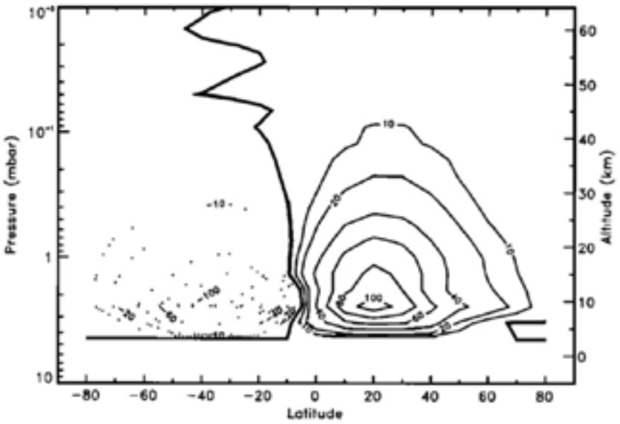

Figure 4c. Mass-weighted stream function, Ψ_m, in units of 10^7 kg/s. Positive values represent clockwise flow, negative contours are dashed, the zero contour is thicker, and the contour interval is nonuniform.

E-P flux divergence (zonal acceleration)

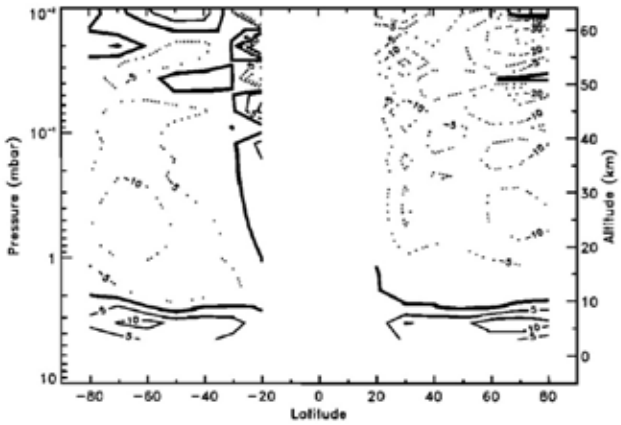

Figure 5. Eliassen–Palm flux divergence $((\rho a \cos\phi)^{-1} \nabla \cdot \mathcal{F})$ in units of $\mathrm{ms^{-1}/d}$. Negative contours are dashed, the zero contour is thicker, and the contour interval is nonuniform.

Meridional circulation of Venus atmosphere

Lee et al. (2015)

temperature field

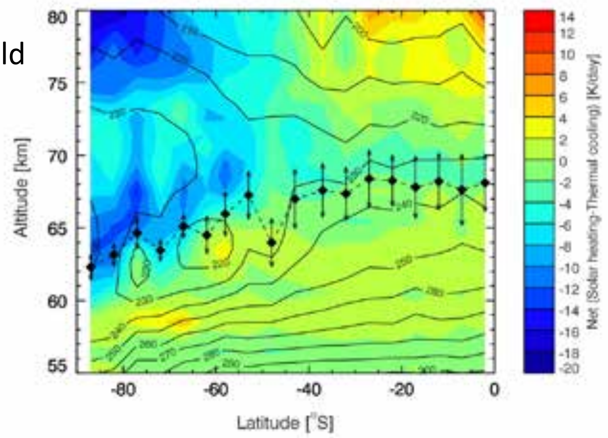

Fig. 14. Latitude–altitude field of the net radiative forcing in the Venus mesosphere. The temperature and cloud top structure are the same as in Figs. 9 and 13.

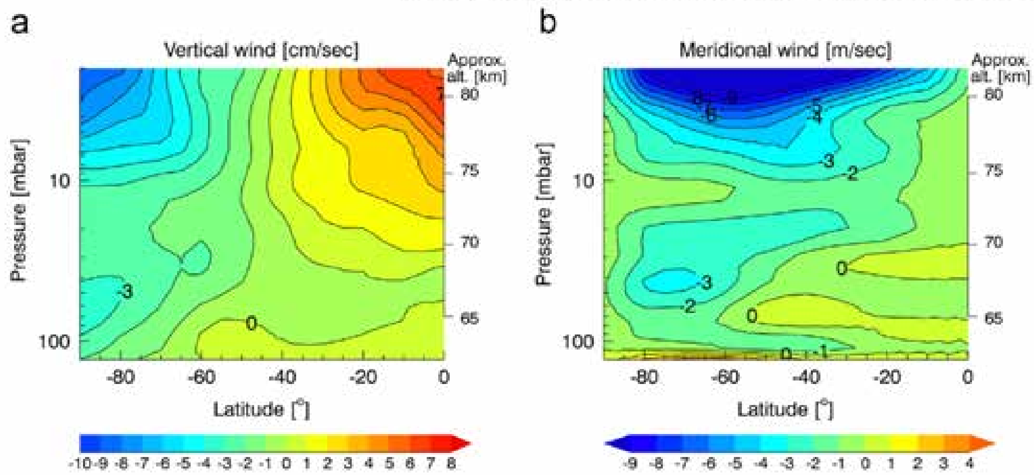

Hot polar dipole & cold collar at Venus's cloud top

Pioneer Venus thermal infrared mapping of the North polar region (Taylor et al. 1980)

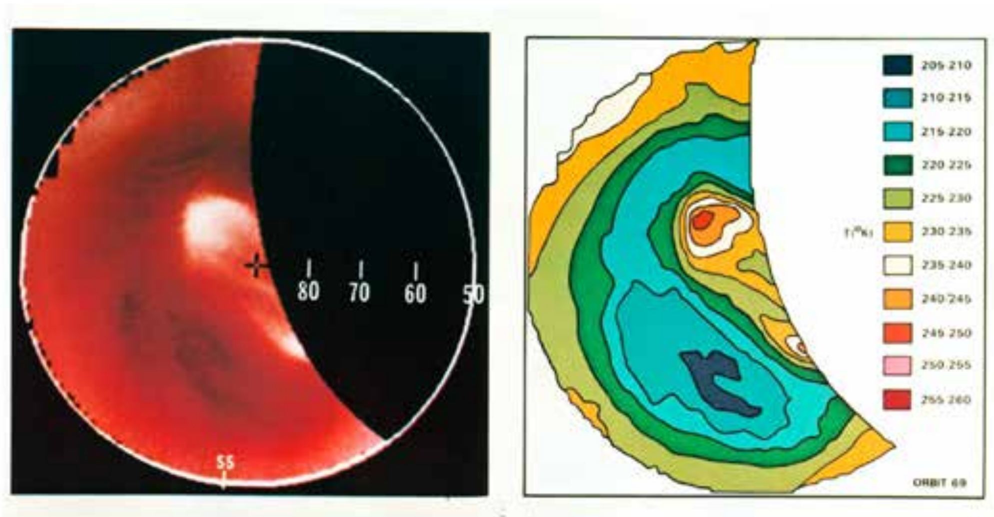

Ando et al. (2016)

With tide

Without tide

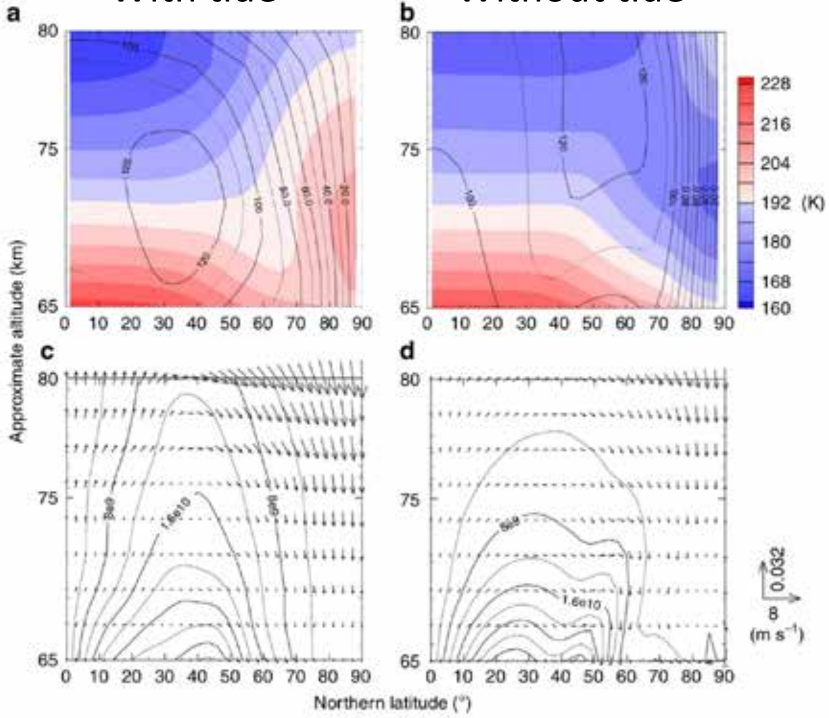

Figure 6 | Meridional cross-sections of the zonally and temporally averaged zonal wind (solid line) and temperature (colour shade) and the horizontal and vertical components of the residual mean meridional circulation (vector) and mass stream fuction (contour). (**a**) Zonal wind and temperature in Case A. (**b**) Those in Case B. (**c**) Residual mean meridonal circulation vector and mass stream function in Case A. (**d**) Those in Case B. Averaged period is two Venusian solar days (234 Earth days) after settling into the quasi-steady state.